USC
UNIVERSITY
OF SOUTHERN
CALIFORNIA

Wednesday, February 27, 2002

School of Engineering

Department of Electrical
Engineering-Systems

Communication Sciences
Institute

Federal Communications Commission
Office of Engineering and Technology
445 12th Street SW
Washington DC 20554

Dear Sirs:

November 16, 2001 was the second anniversary of the experimental license WB2XAM at the University of Southern California. Accordingly I am submitting with this letter a brief report on our activities over the past year, along with copies of the three publications that are referenced in the report. We hope that you find these of use in your continued exploration of UWB radio.

Sincerely,

R. A. Scholtz

Robert Scholtz
Professor

Report to the Federal Communications Commission

from Robert Scholtz, University of Southern California

Experimental License WB2XAM

November, 2001

During the past reporting period we have performed more UWB propagation measurements and produced several technical papers that describe and analyze these measurements. These papers are attached as technical documentation for the work.

Interference Tests in Cooperation with ARRL

We have carried out experiments aimed at quantifying the effect of a UWB signal on a high-quality radio receiver. This work involved UWB radiation in the basement of the EE building at USC and later on top of Parking Structure A (Saturday, Oct. 20, 2001, 9 am - 1 pm). The results of this test, which to some extent illustrate the difficulties in assessing the effect of one specific UWB transmission on a narrowband radio, are described in [1].

UWB Channel Measurements and Modeling

The work of Jean-Marc Cramer on channel modeling, reported last year to the FCC, has been accepted for publication [2].

The UltRa Lab has taken the lead in a DoD sponsored MURI grant for the study of critical problems in short-range UWB radio systems. The prototypical system application is UWB RF tagging.

Our current focus in the propagation area is two-fold: (1) the upgrading of our experimental equipment to conform to anticipated FCC restrictions on UWB radiation, (2) the study of propagation in a warehouse environment, (3) the evaluation of polarization and cross-polarization effects that need to be characterized for randomly-oriented antennas in different environments. The initial antenna structure that we expect to use for the polarization measurements is currently being tested in our new Paul G. Allen Wireless Test Facility, an anechoic chamber that can operate in the 500MHz - 20GHz range.

We have an interest in implementing FCC compliance testing in the anechoic chamber if possible. If you can put us (scholtz@usc.edu) in contact with the cognizant person at the FCC who is developing measurement standards for UWB compliance, we would appreciate it.

UWB Channel Measurements for Ranging

We have performed in-building measurements in support of ranging system design studies. The primary focus is the determination of the portion of the channel response function corresponding to the direct-path signal. Statistics related to the problem of finding the direct path are developed based on these measurements and reported in [3].

Other Work Outside the UltRa Lab

Rob Wilson led a team of student trainees in a propagation experiment on the evening of January 3, 2001, on the 5th floor of the USC Electrical Engineering building (mostly on the north side). The measurements used the Avtech gaussian pulse generator to transmit and the HP DSO to record the waveform for 6 different combinations of trasmit/receive locations, each one with the intervening doors open and closed.

Robert Wilson and Sridhar Ramanujam took the measurements in a fifth floor office (EEB 506) and the adjacent hallway, with one antenna inside the room and the other just outside. They took the measurements on September 29, 2001, from 12 noon to 2pm. They used an Avtech pulser controlled by an Altera FPGA board for generating pulses, with the time-hopping generator set in a non-time hopping mode. This was a test of improvements in the measuring equipment, performed in a typical low-power measurement situation.

References (preprints attached)

[1] R. D. Wilson, R. D. Weaver, M.-H. Chung, and R. A. Scholtz, "Ultra Wideband Interference Effects on an Amateur Radio Receiver,", submitted to the *2002 IEEE Conference on Ultra Wideband Systems and Technologies.*

[2] J.-M. Cramer, R. A. Scholtz, and M. Z. Win,"Evaluation of an Ultra-Wideband Propagation Channel," *IEEE Transactions on Antennas and Propagation,* to appear.

[3] Joon-Yong Lee and R. A. Scholtz,"Ranging in a Dense Multipath Environment using an UWB Radio Link," submitted to *IEEE Journal on Selected Areas in Communications.*

ULTRA WIDEBAND INTERFERENCE EFFECTS ON AN AMATEUR RADIO RECEIVER

R. D. Wilson, R. D. Weaver, M.-H. Chung and R. A. Scholtz

UltRa Lab
Communication Sciences Institute
University of Southern California

ABSTRACT

This paper illustrates the complexity of issues that arise in the accurate measurement and interpretation of ultra-wideband (UWB) interference effects in narrowband receivers. The behavior of an amateur radio receiver in the presence of sinusoidal and UWB interference is studied. We characterize antenna response and receiver non-linearities, which lead to an understanding of UWB effects on the receiver output during outdoor response measurements as a function of range and antenna orientation.

1. INTRODUCTION

Ultra Wideband (UWB) Radio uses radio impulses to transmit information [1]. The key concept underlying UWB radio is that by using low power spread over a very wide bandwidth, one may communicate information without seriously degrading the performance of other narrowband users in the same frequency range. An important area of research in UWB radio is to quantify the effect that UWB transmissions will have on systems with which spectrum is shared. Radio amateurs are one of the groups concerned with this issue because there are bands allocated for amateur radio within the possible range of future UWB systems. This paper describes the results of sensitivity and linearity measurements performed with a receiver system supplied by the American Radio Relay League (ARRL) to quantify the effects of UWB signals. Testing was performed at the University of Southern California (USC), using the experimental UWB transmitter and instrumentation of USC's UltRa Lab. The receiver and its antenna were supplied by the ARRL, which also provided samples of their standard receiver test procedures.

Sophisticated radio amateurs often use their receiving equipment near the limits of its sensitivity in both practical and experimental settings. The Minimum Discernible Signal (MDS) test was suggested by the ARRL [2] as a measure of how strong a desired signal must be in order to be detected. The MDS paradigm provides a useful framework within which to think about the interference problem, in a particular setting. However, one would like to say something more general, namely how much UWB interference will be detected under a range of conditions (UWB source power, range and propagation geometry). This requires a propagation model and an understanding of receiver non-linearities. Early on in our testing, it became clear that we would need to put particular emphasis on characterizing the non-linearities, because our UWB signal was pulsed with high peak-to-average power ratio, and the receiver had quite narrow dynamic range.

This work was supported in part by the National Science Foundation under Award No. 9730556, by the Office of Naval Research through Grant N00014-00-1-0221, by the MURI Project under Contract DAAD19-01-1-0477, and by the Integrated Media Systems Center, an NSF Research Engineering Research Center.

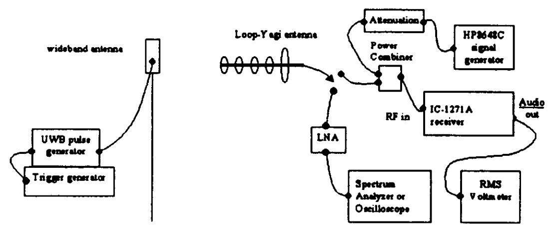

Fig. 1. Experimental setup

2. TESTING PROCEDURES

The test setup is shown in Figure 1. Tests were performed using the UltRa Lab's UWB transmitting equipment, namely a custom-built time hopping trigger generator, an Avtech gaussian pulse generator and a wideband omnidirectional antenna. A variable attenuator was used for power control. The ARRL provided an ICOM IC-1271A receiver and a loop-Yagi antenna as a typical amateur radio setup on which to investigate the interference effects. Details on the UWB signal and antenna characteristics are given in Section 3.

The receiver was operated in the upper-sideband mode, with all other signal processing options, including auto-

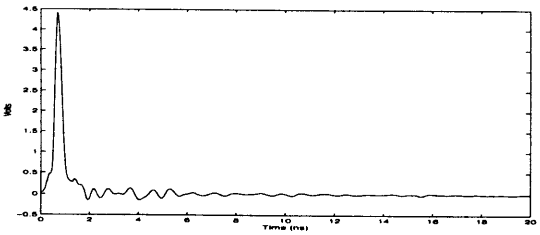

(a) Pulse shape at the pulser output

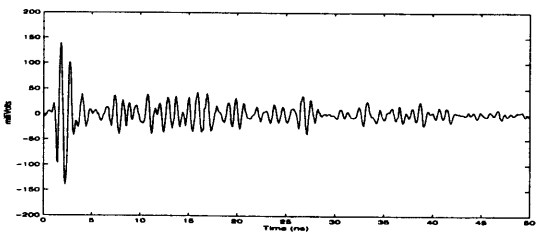

(b) Waveform received by a UWB antenna

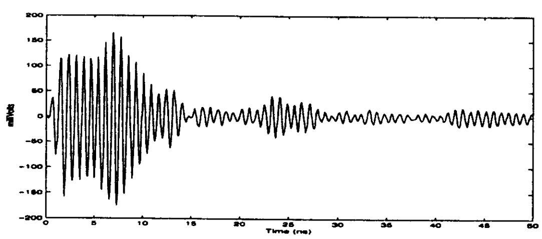

(c) Waveform received by the loop-Yagi antenna

Fig. 2. UWB waveforms

matic gain control, turned off. The RF gain was set at maximum while the audio gain (volume) knob was adjusted so that audio noise output was nominally 30 mV(RMS) when no input was present. The audio "tone" control was set to mid-range. A digital voltmeter was used to measure the audio output.

Testing included signal characterization and linearity tests in a laboratory environment, followed by interference measurements outdoors.

UWB signal characterization was done with a HP54750A high-speed oscilloscope and a HP8563E spectrum analyzer. Since neither instrument has particularly good noise figure, a broadband low-noise amplifier (LNA) was inserted where needed to aid in these characterizations. All measurements are corrected for the gain of the LNA and for cable losses, where applicable.

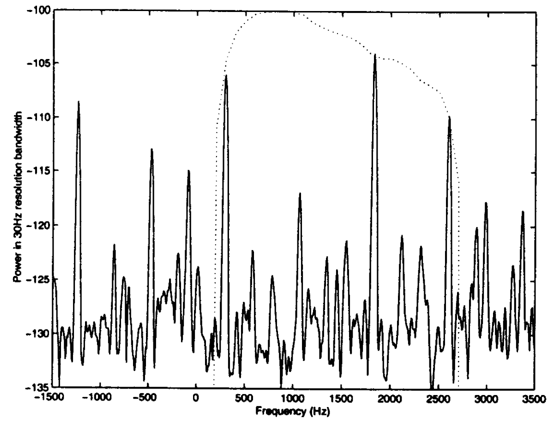

Fig. 3. Narrowband spectrum analyzer trace of the received UWB signal at full power, overlaid with the receiver's audio passband when tuned to 1296 MHz (dotted line, with arbitrary dB offset). The resolution bandwidth is 30 Hz.

To evaluate receiver linearity, the output of the receiver tuned to 1296 MHz was observed over a range of radiated UWB powers, to determine what level of UWB interference will drive the receiver into saturation. As a basis for comparison, the same test was performed using a calibrated continuous wave (CW) input to the receiver, such as to produce a 1000 Hz audio tone.

The MDS is the input signal level required to cause a 3 dB rise in the output audio power with respect to the power when no input is applied. If the receiver is operating linearly, it is a measure of the input noise-plus-interference power within the passband of the receiver. Therefore, measuring the output power of the receiver, in linear response conditions, also yields the MDS if the receiver gain is known.

3. SIGNAL AND ANTENNA CHARACTERISTICS

The elementary UWB signal used in these tests is a gaussian pulse of approximately 0.7 ns duration at 50% amplitude and with 90% bandwidth of 1.5 GHz. The pulse shapes at the output of the pulser, after transmission between two ultra-wideband diamond-dipole [5] antennas, and after transmission between one diamond dipole and the loop-Yagi are shown in Figures 2(a), (b) and (c), respectively.

The time-average pulser output power is -10.3 dBm in the time-hopped mode, including transmission line losses between the pulser and transmit antenna. The time hopping system generates a sequence of 1023 pulses, randomly pulse position modulated at an average interval of $1.27\mu s$, thus producing an overall waveform period of 1.3 ms. In Figure 3, the UWB spectrum is shown over a 4 kHz range about 1296 MHz, measured between a wideband diamond-dipole transmit antenna and the loop-Yagi receive antenna at a separation of 3 m. Overlayed is the measured frequency response of the ICOM receiver when tuned to that frequency, plotted on an arbitrary dB scale.

Because of its periodicity, the UWB test signal has a line spectrum. The 1.3 ms period indicates that we should expect spectral lines at intervals of approximately 770 Hz. The expected 770 Hz spaced lines are apparent, as are other, generally weaker, lines due to idiosyncracies of the transmitter hardware. All measurements were performed using no data modulation. Random data modulation will disrupt the periodicity of the signal and therefore further smooth the distribution of power over frequency.

The UWB antenna gain pattern and frequency response are plotted in Figure 7(a). Its polarization is vertical. The gain pattern and frequency response of the loop-Yagi antenna are shown in Figure 7(b). Its polarization was found to be nearly linear and it was oriented for maximum response. To ensure repeatable results, the loop-Yagi was pointed directly at the UWB antenna during signal characterization and linearity testing.

4. EXPERIMENTAL RESULTS

In Figure 3, we can see how the UWB spectrum relates to the passband of the receiver tuned to 1296 MHz. There are four major spectral peaks within the receiver passband. As the receiver is tuned, a different number of peaks may enter the band and the detected interference power may change. Because the receiver passband is approximately 2.5 kHz, and the peaks are spaced at 770 Hz intervals, there will always be three or four peaks within the passband, so we should expect a variation in interference level of about 4/3 or 1.25 dB, plus any variations due to the shape of the signal spectrum itself. We will see in section 4.2 that the interference level varies about 3.5 dB when receiver response is linear.

4.1. Receiver Linearity

The receiver linearity was characterized for both UWB and sinusoidal signals. In Figure 4 we see that the receiver behaves differently in each case. The response due to the calibrated CW source may be considered as firmly known, while the horizontal alignment of the UWB curve was more difficult to establish. It involves estimating the portion of input power, already filtered by the antennas, contained within the passband of the receiver. This may be done by reference to Figure 3, or using the time domain waveform of Figure 2(c). In the latter case, we can estimate the average

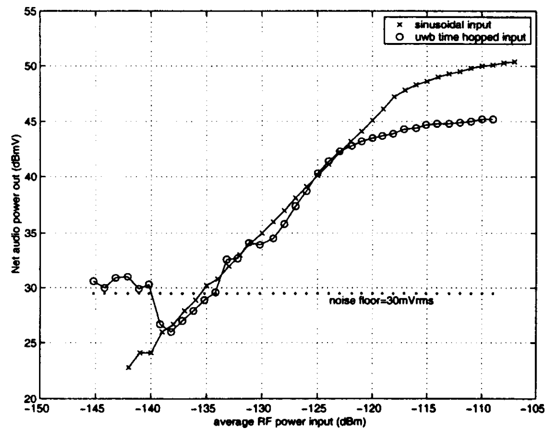

Fig. 4. Receiver linearity at maximum RF gain. Antenna separation was 2 m for the UWB case.

power in the passband of the receiver by taking a discrete Fourier transform and using our knowledge of the average pulse period. By this method, at full transmitter power (the rightmost point in Figure 4), the average received UWB power within the receiver passband is approximately -107 dBm, which justifies the horizontal positioning of the UWB curve to within 2 dB.

Assuming that our placement of the UWB curve is correct, the plot shows that the receiver begins to behave non-linearly at approximately 5 dB lower average input power when the UWB signal is present compared to the sinusoidal signal. Also note the 5 dB lower compressed output level for the UWB signal. This is thought to be due to the low duty cycle of the pulse waveform, in that the receiver is in compression due to the high peak power, but this amount of power is not always present as it would be in a sinusoidal signal. For some portion of the time between pulse arrivals the input power is much lower than the peak and the receiver is not saturated, therefore although the response is non-linear, the average output power is reduced.

The 5 dB difference in both the compressed output power and the saturation point suggests a duty cycle for the UWB waveform within the receiver of approximately 30% at the point where compression occurs. This indicates that the pulses are undergoing compression in an early IF stage with bandwidth of about 2.5 MHz. With the receiver in compression, the measured interference level is lower than would be the case if response were linear. The compressed receiver stage acts as a bandpass limiter, which is well known to help reduce the effects of pulsed interference. A lower duty cycle UWB signal of equal average power, whose higher peak power would be compressed in an earlier receiver stage, would produce even less output interference.

The UWB linearity plot shows that the receiver will op-

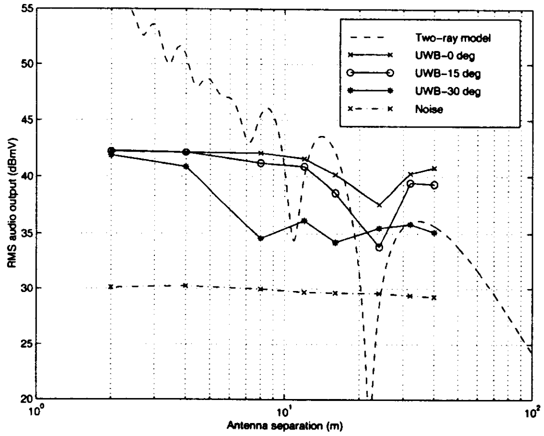

Fig. 5. Measured audio output vs. range and antenna boresight angle. An idealized two-ray model is shown for comparison.

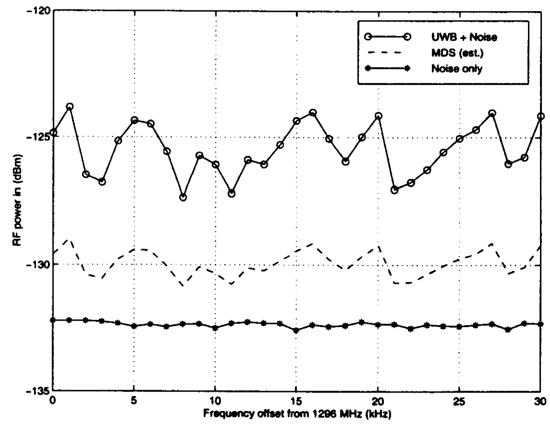

Fig. 6. Outdoor UWB response measured at 24 m range and 30 degrees off boresight. The MDS estimate is corrected for the excess power of our transmitter.

erate linearly if the input power is reduced by at least 15 dB. Therefore, increasing antenna separation to a minimum of approximately 12 meters in free space should also result in linear operation. This estimate of minimum separation is supported in the following section.

4.2. Outdoor Measurements and MDS Estimate

Outdoor tests were performed to confirm ranges and antenna orientations where the receiver could be expected to behave linearly. This was done on the top floor of a parking structure at USC. In addition to the direct path and the ground reflection, there may have been other significant reflections due to perimeter walls and metal fences. The audio output of the receiver was measured at different separations and the receiving loop-Yagi antenna was pointed 0, 15 and 30 degrees away from the transmit antenna, with the UWB signal at full power. The results are shown in Figure 5. Here, measured noise is subtracted from the UWB measurements.

Also plotted are the predictions of a simple two-ray model over an ideal ground plane, modified from [3]. The model assumes idealized antenna patterns similar to Figure 7 and linear response extrapolated from Figure 4. Clearly the model does not match the measurements very well, but it does provide a useful frame of reference in which to interpret our results. Viewed in this light, the data support our expectation that audio output is compressed to a constant for separations less than about 12 meters with the loop-Yagi antenna boresighted, due to the non-linearity of the receiver. The presence of a shallow null near 20 meters also suggests that we are on the right track, but that the reflected ray is considerably weaker than is assumed by the model.

Having determined the minimum antenna separation required by the receiver to operate linearly, we performed a final series of measurements aimed at estimating the MDS. We chose a 24 meter separation, with the receiving loop-Yagi antenna pointed 30 degrees away from the UWB transmitter. The test was done over a 30 kHz span in 1 kHz steps beginning at 1296 MHz, with the UWB signal alternately turned on and off. The results are shown in Figure 6. The scaling of the vertical axis is based on Figure 4. The UWB signal produced an output power 5 to 8 dB above the receiver noise floor, while the noise varied less than 1 dB. The variability of the UWB-induced output is due to the line spectrum of the UWB signal.

5. COEXISTENCE AND REGULATION

In this paper, we studied the behavior of an amateur radio receiver in the presence of the UWB interference. It is important to understand the limitations of the data presented above.

Our UWB signals did not conform to proposed UWB regulatory limits on average power spectral density [6]. The limit, below 2 GHz, is 12 dB below 500 μV/m into any 1 MHz of bandwidth at 3 m. Our calculations show that our output at 1296 MHz was 287 μV/m per MHz, or roughly 7 dB higher. Figure 6 shows our best estimate of what the receiver's MDS might have been if our transmitter had been in compliance with the proposed limit.

Test configurations were chosen, not as realistic interference scenarios, but rather to facilitate obtaining reasonably clean and repeatable measurements and to achieve an understanding of potentially important effects. Pointing a beam antenna directly at the source of UWB interference at close range in an enclosed space, as we did, is a good way to measure interference effects, but the results cannot be taken as a direct illustration of the impact of UWB on amateur radio in general.

Despite our emphasis in this paper on characterizing and later avoiding non-linearities in receiver response measurements, one should not assume that this non-linear behavior is undesirable. To the contrary, in this case, a high peak-to-average power ratio UWB signal caused less interference than did a CW input having equal average power in-band, as was pointed out in Section 4.1. Notwithstanding any other considerations motivating FCC's proposed limits on peak-to-average power ratios, this narrowband receiver system would probably benefit from an even higher ratio. Since the pulse width seen by the receiver is effectively set by its antenna, this might mean raising the UWB pulse amplitude while slowing the pulse repetition frequency to maintain the same average power level.

Acknowledgments

The authors wish to thank ARRL, and particularly Ed Hare for the use of their receiver. Thanks are also due to S. Chang, C.-C. Chui, M. Nemati, S. Ramanujam and R. Tarif for their help with the experiments.

6. REFERENCES

[1] R. A. Scholtz and M. Z. Win, "Impulse Radio," invited paper, *Proc. PIMRC'97*, Sep 1997.

[2] M. Tracy and M. Gruber, *Test Procedures Manual, Rev. F*, American Radio Relay League, June 2000.

[3] T. S. Rappaport, *Wireless Communications: Principles & Practice*, Prentice Hall, 1996.

[4] R. A. Scholtz et. al., "UWB Deployment Challenges," invited paper, *Proc. PIMRC'00*, Sep. 2000.

[5] H. G. Schantz and L. Fullerton, "The Diamond Dipole: A Gaussian Impulse Antenna," *Proc. IEEE AP-S Int. Symp.*, July 2001.

[6] Federal Communications Commission, "Revision of Part 15 of the Commission's Rules Regarding Ultra-Wideband Transmission Systems," *NPRM 00-163*, May 10, 2000.

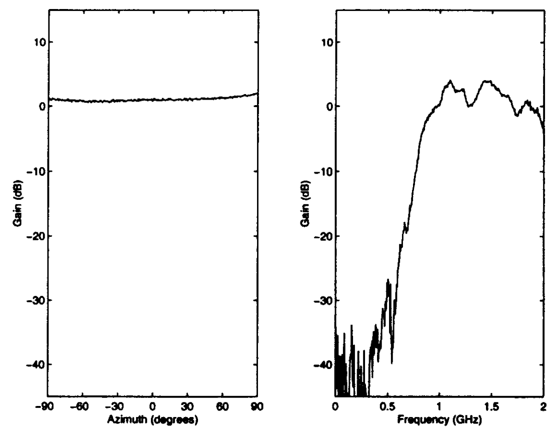

(a) UWB antenna

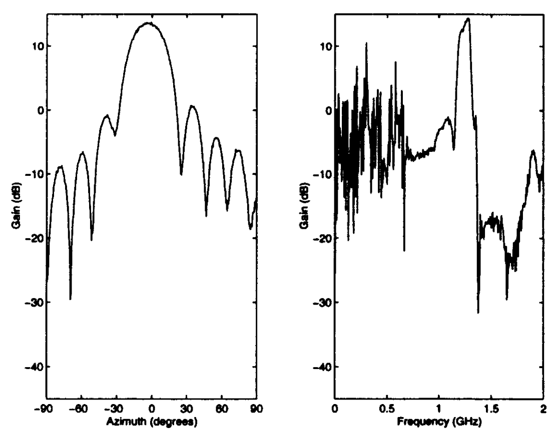

(b) 14-element loop-Yagi antenna

Fig. 7. The 1296 MHz azimuth pattern and boresight frequency response of the two antennas

Evaluation of an Ultra-Wideband Propagation Channel

J.M. Cramer, R.A. Scholtz, M.Z. Win

Abstract— **This paper describes the results of an ultra-wideband (UWB) propagation study in which arrays of propagation measurements were made. After a description of the propagation measurement technique, an approach to the spatial and temporal decomposition of an array of measurements into wavefronts impinging on the receiving array is presented. Based on a modification of the CLEAN algorithm, this approach provides estimates of time-of-arrival, angle of arrival, and waveform shape.**

This technique is applied to 14 arrays of indoor propagation measurements made in an office/laboratory building. Statistical description of the results is presented, based on a clustering model for multipath effects. The parameters of these statistical models are compared to results derived for narrowband signal propagation in the indoor environment.

I. Ultra-Wideband Radio

An ultra-wideband (UWB) radio signal is one whose fractional bandwidth (i.e., its 3 dB bandwidth divided its center frequency) is large, typically over 0.25. Such signals are generated by driving an antenna with very short electrical pulses (on the order of a few nanoseconds to fractions of a nanosecond in duration). Hence these radio systems often are referred to as short-pulse or impulse radio systems. Typically the radiated pulse signals are generated without the use of local oscillators or mixers.

The antennas in UWB systems are significant pulse-shaping filters. In addition, many environments provide a wealth of resolvable multipath. As a result, the received signal often bears little resemblance to the signal driving the transmitter's antenna. If the result of an impulse transmission in free space is a received waveform $p(t)$, then in a typical environment, a typical multipath model for the signal $r(t)$ received over an indoor propagation channel is

$$r(t) \approx \sum_n a_n\, p(t-\tau_n)\,, \qquad (1)$$

with a_n and τ_n representing the amplitude and relative delay of the n^{th} component of the received signal. This is a considerably simplified model of reality that is best interpreted as saying that the signal $r(t)$ can be represented as a weighted sum of time-shifted versions of the waveform $p(t)$, without attempting to make strong connections between a_n and τ_n and the physical environment. This model's value is in designing a radio receiver for a digital communication system using modulations constructed from similar pulse sources driving a similar antenna system in a similar environment.

It is more common for a_n and τ_n to be referred to as the amplitude and delay of the n^{th} propagation path, suggesting a more physical interpretation of the environment. This physical interpretation of the channel model is questionable for several reasons. When a wave reflects off an object or penetrates through a material in the process of "multipath" propagation, the effects are frequency sensitive and therefore the waveform is filtered in some way, and the resulting single "multipath component" may actually be represented by several or many terms in the model for $r(t)$. This suggests that a channel model for UWB signals that is more closely related to physical propagation paths should be of the form

$$r(t) \approx \sum_n a_n\, p_n(t-\tau_n)\,, \qquad (2)$$

where now the pulse shape associated with a propagation path is dependent on that path. Even more perplexing is the fact that if an antenna is electrically large (e.g., compared to the wavelength of the center frequency of the received signal) the waveforms radiated in different directions from the transmitted antenna look considerably different in the far field [6], and undergo similar direction-dependent distortions on reception. This effect also could be imbedded in a model with path-dependent pulse shape.

A number of propagation studies have been reported, for both indoor and outdoor environments [2], [4], [5], [7], [8], [14], [17], some examining just the temporal properties of the channel and some characterizing the spatio-temporal channel response. The results of these studies may not adequately reflect the special bandwidth-dependent effects associated propagation of UWB signals.

II. An UWB Propagation Experiment

The propagation experiment that we analyze here used two vertically polarized diamond-dipole antennas [9], each 1.65 meters above the floor and 1.05 meters below the ceiling in an office/laboratory environment [21]. The equivalent received pulse at 1 meter in free space can be estimated as the "direct path" signal in an experiment in which there is no multipath signal at small relative delays from the direct path signal. This received waveform, embodying char-

This work was funded in part by the National Science Foundation under Award No. 9730556 and in part by the TRW Space and Electronics Group.

Jean-Marc Cramer is with TRW Space and Electronics, Redondo Beach, CA 90278, USA. E-mail: jean-marc.cramer@trw.com

Robert Scholtz is with the Communication Sciences Institute, EEB 500, Department of Electrical Engineering - Systems, University of Southern California, Los Angeles, CA 90089-2565 USA. E-mail: scholtz@usc.edu

Moe Win is with the Wireless Systems Research Department Newman Springs Laboratory, AT&T Labs-Research, Rm 4-147, 100 Schulz Dr., Red Bank, NJ 07701-7033, USA. E-mail: win@research.att.com

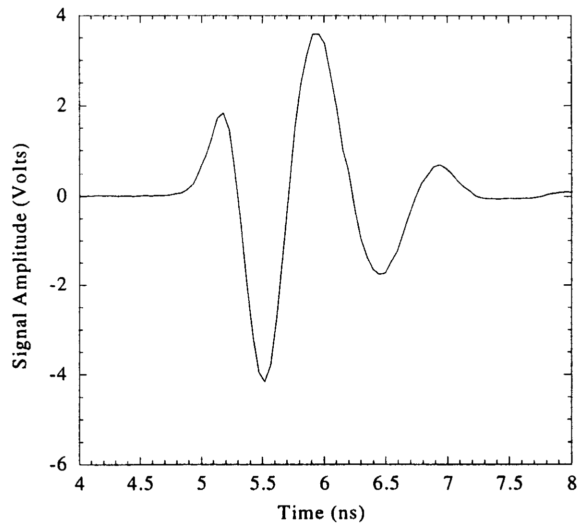

Fig. 1. Transmitted pulse shape captured at 1 meter separation from the transmit antenna

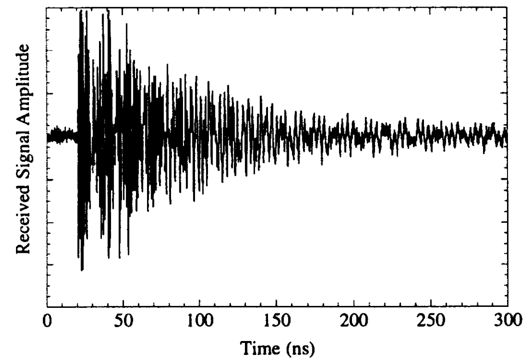

Fig. 2. Received signal on a single sensor at location P

acteristics of the antenna system and pulse driver, is shown in Figure 1.

The placement of the transmitter and various receiving antenna positions are shown on a floor plan in Figure ??. The building construction is steel stud and dry wall. A typical pulse-induced channel response function is shown in Figure 2. In the experiment, rectangular arrays of measurements are made by moving the receiving antenna to the 49 points in a 7×7 array with 6 inch spacing. Hence each measurement array covers one square yard, and 14 such arrays of measurements are taken at the locations marked on Figure 3. The experimental arrangement included a stable clock that triggered both the receiver (a sampling oscilloscope) and the transmitting pulser. This receiver timing control allowed the sequence of measurements composing the array to be interpreted as simultaneous measurements so that array processing could be used to analyze spatial properties of the received signal. Buried in this approach is the assumption that the environment does not change while the sequence of measurements is being made, and that the receiving antenna support structure, etc., does not significantly affect the measurement. One such array of time-response measurements has been animated and is displayed at `http://ultra.usc.edu/ulab/`.

Several measurement traces and the results of data analysis of individual measurements in this collection (e.g., variations in total trace energy across the array, the effective bit-error rate achieved by an L-tap selective Rake receiver in some array measurement locations as a function of L) are presented in [21].

III. Structure of the CLEAN Algorithm

Our approach to the data analysis uses a variation of the CLEAN algorithm to process arrays of UWB measurements with a minimum of *a priori* information. Initially used to enhance radio astronomical maps of the sky [3], the CLEAN algorithm also has been used in more narrowband communication channel characterization problems [14], [18]

As applied here, the CLEAN algorithm uses delay-and-sum beamforming to construct the beamformer's response as a function of beam direction and time. The beam direction and time giving maximum response are found and a UWB pulse signal is assumed to be present at that time. The only assumption made about the structure of the signal is that it exists within a small window of time at the beamformer output. No canonical wave shape (e.g., the $p(t)$ assumed in (1)) was assumed. Here we develop a directional version of the model in (2) in which different waveform shapes are allowed for different values of n.

We refer to the variant of the CLEAN algorithm used here as the Sensor-CLEAN algorithm, since the relaxation step takes place on the sensor data directly, rather than on the beamformer output. This algorithm is summarized by the following steps.

Sensor-CLEAN Algorithm

1. Input : Digitized pulse response functions in the form of N-tuples from M different sensors; loop gain factor γ (algorithm parameter); the relaxation window half-width T_p in samples; a detection threshold T_{det} which is used to control the stopping time of the algorithm; the set of beam pointing angles (azimuth θ_j, elevation ϕ_j), defining the J beampointing directions that discretize the angle of arrival search space.
2. Initialize : Form an MN-dimensional measurement vector $\mathbf{d}(0)$ (the initial residual data vector) by concatenating the N-tuples of waveform time samples for each of M antenna (sensor) positions. Construct the delay-and-sum beamforming matrix $\mathbf{B}$ such that

$$\mathbf{s}(0) = \mathbf{B}\mathbf{d}(0)\,, \tag{3}$$

where the $n+N(j-1)^{\text{th}}$ element of $\mathbf{s}(0)$ is the output of the j^{th} beam at sample time n, associated with beamforming at azimuth angle θ_j and elevation angle ϕ_j. (The $JN \times MN$ beamforming matrix $\mathbf{B}$ need only be constructed once.) Set

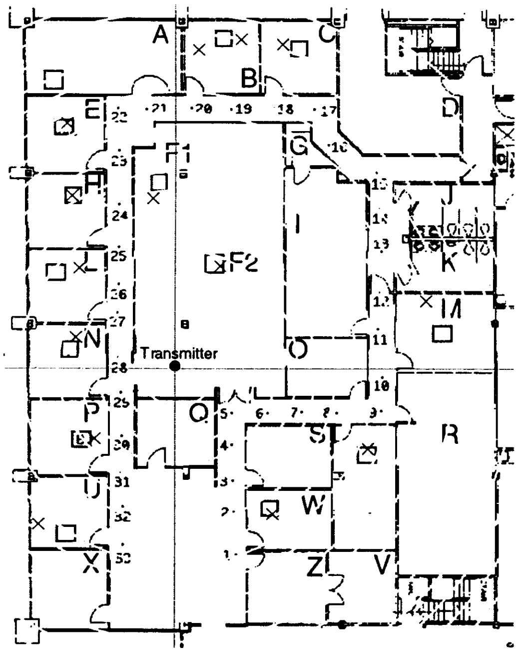

Fig. 3. Measurement floor plan with concentric circles spaced 1 meter apart, centered at transmitter, and measurement array locations indicated by labeled squares. Estimated locations of the measurement sites, determined from the recovered signal information, are indicated by an $\times$.

the iteration counter i to $i = 0$. Set the detection list $\mathcal{D}$ to the empty list.

3. Signal Detection : Find the index k_{i+1} of the entry which has maximum magnitude in the modified beamformer output $s_k(i)$.

$$k_{i+1} = \operatorname{argmax}_{1 \le k \le JN} |s_k(i)| \,. \tag{4}$$

The entry having maximum magnitude is

$$a_{i+1} = s_{k_{i+1}}(i) \tag{5}$$

If the largest signal is below threshold, i.e., $|a_i| < T_{\mathrm{det}}$, then set the number of iterations $I = i$ and STOP.

4. Increment the iteration counter : $i \rightarrow i + 1$.

5. Window the array data : Form the i^{th} mask vector $\mathbf{b}_i$, an MN dimensional vector to be used to mask the i^{th} residual data vector. The mask $\mathbf{b}_i$ has a 1 in every sensor data position which was used to compute the delay-and-sum beamformer output in the range $s_{k_i - T_\mathrm{p}}(i), \ldots, s_{k_i + T_\mathrm{p}}(i)$. Mask the residual sensor data to extract the data affecting the i^{th} detected waveform by constructing the MN dimensional vector $\mathbf{b}_i \otimes \mathbf{d}(i-1)$, where $\otimes$ represents the element-by-element multiplication of the two vectors.

6. Residual Beamform : Reduce the residual sensor data vector by a fraction $1 - \gamma$ to produce the residual data vector for the next iteration.

$$\mathbf{d}(i) = \mathbf{d}(i-1) - \gamma\, \mathbf{b}_i \otimes \mathbf{d}(i-1) \tag{6}$$

and regenerate the residual beamformer output

$$\mathbf{s}(i) = \mathbf{B}\mathbf{d}(i) \,. \tag{7}$$

7. Detected signal storage : Append $\{a_i, \theta_i, \phi_i, t_i, \mathbf{w}(i)\}$ to $\mathcal{D}$, where $\mathbf{w}(i)$ is the waveform detected at the beamformer output and removed on the i^{th} iteration,

$$\mathbf{w}(i) = \gamma(0 \ldots, 0, s_{k_i - T_\mathrm{p}}(i), \ldots, s_{k_i + T_\mathrm{p}}(i), 0, \ldots, 0)^{\mathrm{t}} \tag{8}$$

where $k_i = t_i + [j_i - 1]\, N$ and $0 \le t_i < N$, and θ_i and ϕ_i are the azimuth and elevation angles of beam j_i.

8. Iterate : Go to step 3.

End Sensor-CLEAN

The convergence of the Sensor-CLEAN algorithm is guaranteed through a monotonic reduction in the residual energy on each iteration. As with most indirect algorithms, the solution generated by the Sensor-CLEAN algorithm is not unique; it is a function of the input parameters, in this case γ, T_p, and T_{det}, as well as the measured data. The algorithm parameters must be selected based on some criterion which generally trades estimate fidelity against computation time.

Since the precise shape and duration of the received signals is not known a-priori, the Sensor-CLEAN algorithm described above was applied to the measured data multiple times with different relaxation windows, to better match the processing to the anticipated variations in the received signals. Each of these applications results in a list $\{a_i, \theta_i, \phi_i, t_i, \mathbf{w}(i)\}_{i=1}^{I}$ of the amplitude a_i, the azimuth look direction θ_i, the elevation look direction ϕ_i, the time-of-arrival, t_i and the waveform $\mathbf{w}(i)$ recovered on each iteration. A post-processing algorithm also was developed to combine elements of each resulting detection list into a final list of resolvable signal arrivals.

For the results presented below, the beamformer output was generated at 1^o increments in azimuth, and the following nineteen elevations angles are used: 90^o, 88^o, 86^o, 84^o, 82^o, 80^o, 78^o, 76^o, 74^o, 72^o, 70^o, 65^o, 60^o, 55^o, 50^o, 45^o, 40^o, 30^o, 20^o. The three Sensor-CLEAN relaxation windows of $T_p = \pm 6$ samples, $T_p = \pm 8$ samples and $T_p = \pm 12$ samples are used, with $\gamma = 0.10$ and a detection threshold of 0.104 volts. The three relaxation windows and the value of γ were selected to balance algorithm performance and computation time. The detection threshold was chosen to give the algorithms a 30 dB range between the largest and smallest recovered signals at Location P.

IV. Application of Sensor-CLEAN to the Measured Data

The Sensor-CLEAN algorithm and the post-processing algorithms were applied to the measured propagation data. In this section, channel models for UWB signal propagation in an indoor environment are proposed. The primary goal of this effort was to develop models by which quantitative comparisons of the UWB channel with more narrowband indoor propagation results [2], [5], [7], [8], [14] could be made and the performance of UWB communication systems could be predicted. A secondary goal was to use the

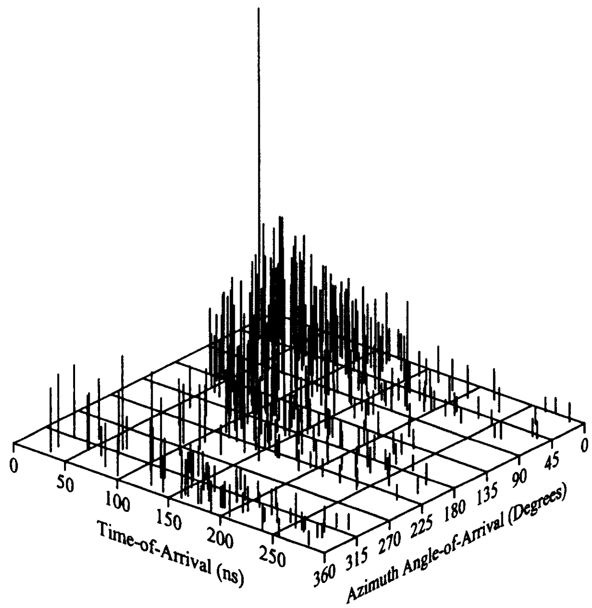

Fig. 4. Recovered signal location and amplitude information at location P.

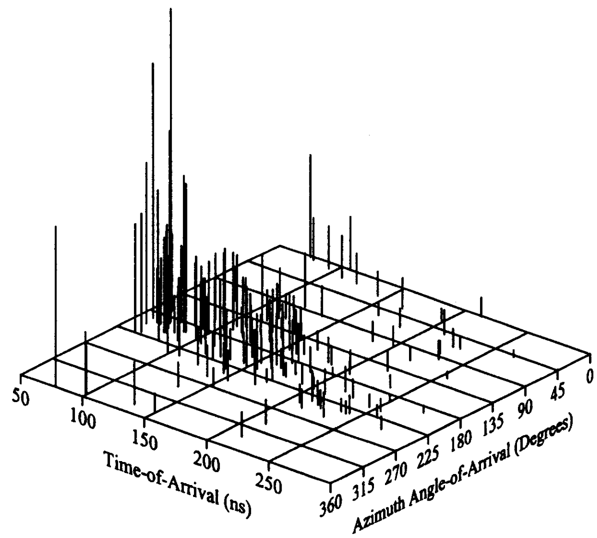

Fig. 5. Recovered signal location and amplitude information at location B.

output of the processing algorithms to study the effects of propagation on the transmitted UWB signals.

The floor plan of the building in which the measurements were made is shown in Figure 3, with the actual location of the measurement arrays indicated by the squares. The recovered measurement locations, indicated by an $\times$ in each room, were determined by the time-of-arrival and azimuth angle-of-arrival of the first incident signal in time recovered by the Sensor-CLEAN and post-processing algorithms. The corresponding direct path length was calculated according to

$$d_{LOS} = (n_1 - n_d) \times c/f_s + 1 \text{ meters} \tag{9}$$

where n_1 is the sample at which the direct-path signal arrives, $n_d = 122$ is the known propagation delay in samples at a 1 meter separation between the transmitter and the receiver, c is the speed of light and f_s is the sampling frequency. With the exception of the result at location A in the building, where the signal strength is weak and the interference is high, the calculated measurement locations correlate reasonably well with the floor plan.

The scatter plots of Figure 4 - Figure 7 display the location of the recovered signal in the time and azimuth plane, and the height of the line is proportional to the amplitude of the recovered signal. Dependence on the elevation angle has been suppressed. In most figures, the existence of clusters of arrivals can be seen, some locations exhibiting a stronger clustering effect than others. These clusters are determined by large scale building features such as the walls, doors and hallways.

The algorithms also recover signal waveform information, and in particular, the direct path waveform recovered at each of the measurement locations was recorded. This gives some insight into the effect of this indoor propagation channel on the transmitted UWB waveforms. For comparison purposes, consider first the signal recorded at a 1 meter separation between the transmitter and the receiver, shown in Figure 1.

Given the transmission of this signal and the processing described above, some of the recovered direct path waveforms are shown below in Figure 8 - Figure 9.

The recovered direct path waveforms are shown in Figure 8 and Figure 9. Each of the waveform plots displays two curves, corresponding to the waveform recovered by the processing algorithms using time windows of different sizes. A larger window has the advantage of giving a more complete picture of isolated signals, while a smaller window may be more successful in resolving dense multipath. Note that there is a progressive distortion of the signal when viewed at 1 meter (Figure 1), shadowed in the same room (Figure 9) and through walls (Figure 8).

V. Clustering Models for the Indoor Multipath Propagation Channel

Previous models for the indoor multipath propagation channel [2], [5], [8], [14], [15] have reported a clustering of multipath components, in both time and angle. In the model presented in [14], the received signal amplitude, β_{kl}, is a Rayleigh distributed random variable with a mean-square value that obeys a double exponential decay law, according to

$$\overline{\beta_{kl}^2} = \overline{\beta^2(0,0)} e^{-T_l/\Gamma} e^{-\tau_{kl}/\gamma} \tag{10}$$

where $\overline{\beta^2(0,0)}$ describes the average power of the first arrival of the first cluster, T_l represents the arrival time of the l^{th} cluster, and τ_{kl} is the arrival time of the k^{th} arrival

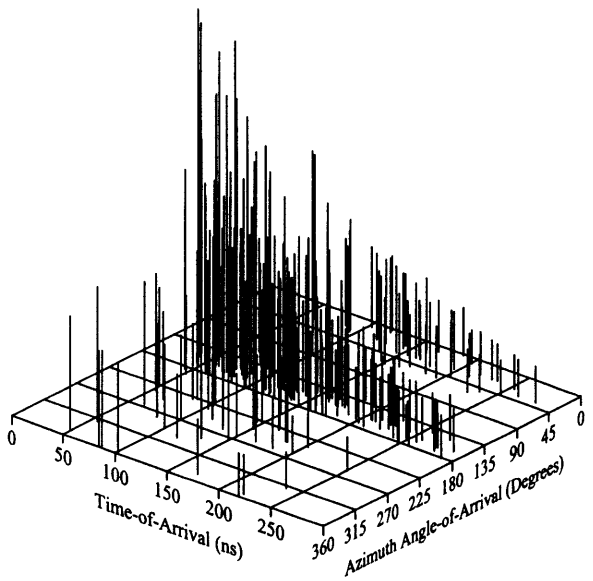

Fig. 6. Recovered signal location and amplitude information at location H.

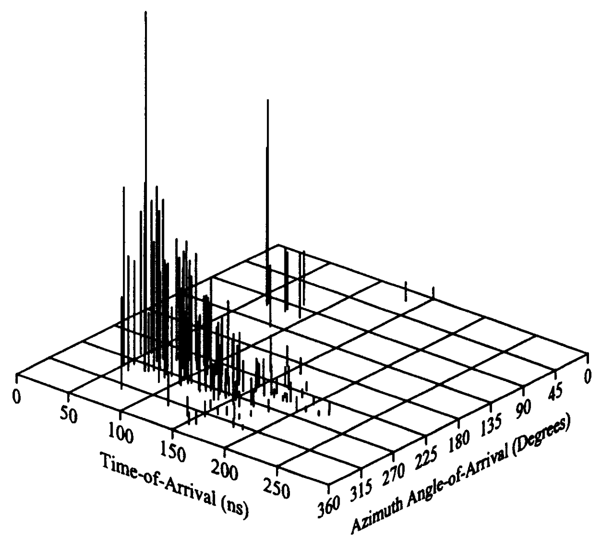

Fig. 7. Recovered signal location and amplitude information at location M.

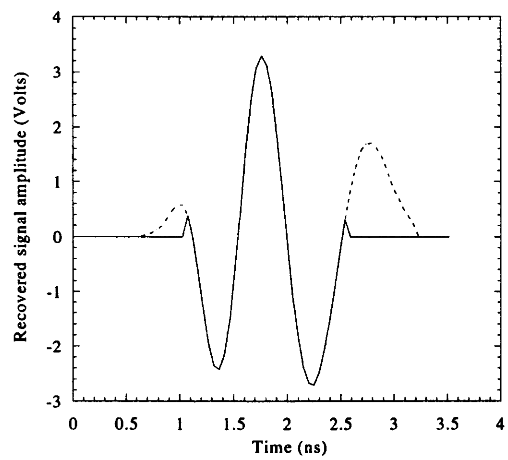

Fig. 8. Recovered direct path waveform at location P.

within the l^{th} cluster, relative to T_l. The parameters Γ and γ determine the inter-cluster signal level rate of decay and the intra-cluster rate of decay, respectively. The parameter Γ is generally determined by the architecture of the building, while γ is determined by objects close to the receiving antenna, such as furniture. The results presented in [14] make the assumption that the channel impulse response as a function of time and azimuth angle is a separable function, or

$$h(t, \theta) = h(t)\, h(\theta) \tag{11}$$

from which independent descriptions of the multipath time-of-arrival and angle-of-arrival are developed. This is justified by observing that the angular deviation of the signal arrivals within a cluster from the cluster mean does not increase as a function of time.

Following this model, and based upon the apparent existence of clusters in the UWB channel seen in Figure 4 - Figure 7, UWB channel models which account for the clustering of multipath components are developed here. As was noted in [14], it is very difficult to develop a robust algorithm for the automatic identification of cluster regions. Here, cluster regions were selected manually by considering both sliding window plots of the arrival density (in time and angle), an example of which is shown in Figure 10, and scatter plots of the time and azimuth angle-of-arrival. In all, 65 clusters were identified in the recovered signals for the fourteen measurement locations.

Following the identification and sorting of the cluster information, the reference arrival, i.e., the earliest arrival in each cluster, was identified, and a decay exponent was determined, again following the methodology in [14]. The time of the first arrival within the cluster is set to zero, and all other arrivals are reported relative to this time. The recovered energy in the collection of signals is also reported relative to the energy in the first arrival in the first cluster, which is normalized to 1, and is referred to as the normalized relative energy, as in [14].

With the measurements at locations A and E excluded because of their low signal-to-noise ratio, the resulting UWB cluster energy versus relative delay models for the indoor channel are shown below in Figure 11 and Figure 12. The first plot reports the decay of the energy in the recovered waveforms, and the second reports the energy as a function of the recovered amplitude only, under the assumption that all incident waveforms are identical. Several values for the decay exponent Γ are shown for each plot, in order to demonstrate the consistency of the results. Γ_{med} is the median and Γ_{mean} represents the mean of the val-

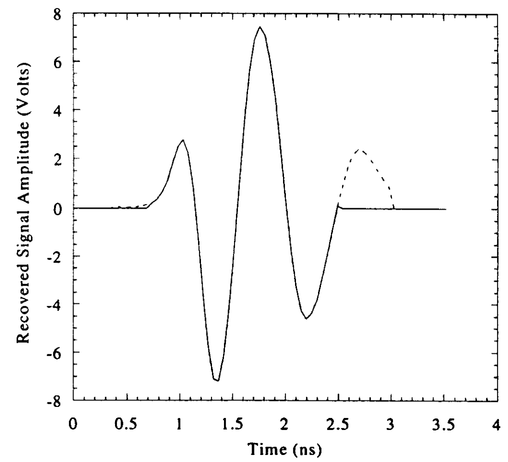

Fig. 9. Recovered direct path waveform at location F2.

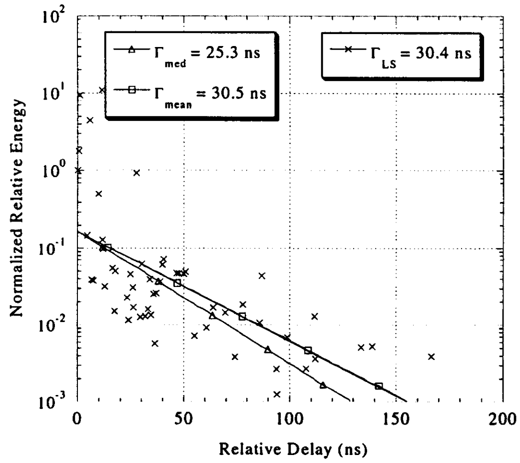

Fig. 11. Inter-cluster loss vs. relative delay when considering the energy in the recovered waveforms (energy of first arrival within a cluster).

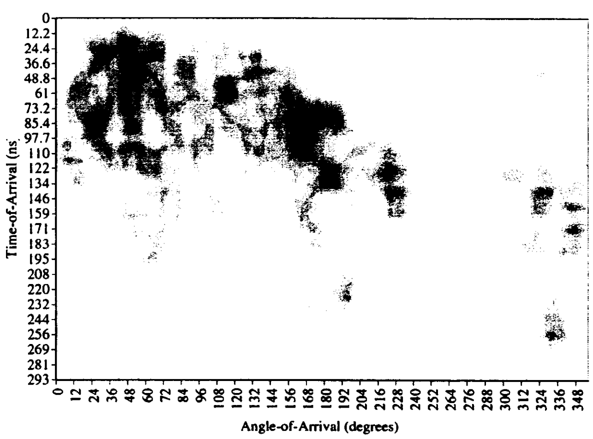

Fig. 10. Density of signal arrivals over time and azimuth angle at location P.

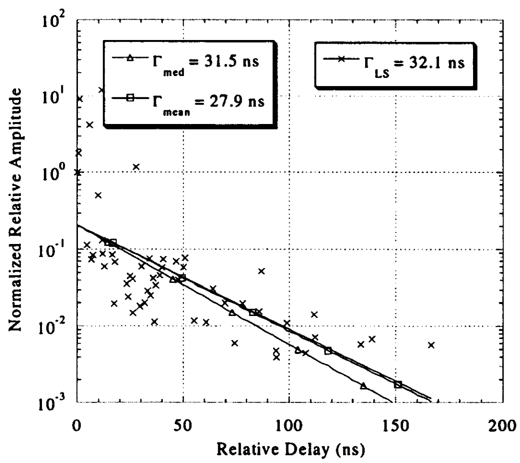

Fig. 12. Inter-cluster loss vs. relative delay when considering the amplitude of the recovered waveforms (amplitude of first arrival within a cluster).

ues obtained by considering the best-fit line for each measurement location individually. Γ_{LS} is the exponent of the best fit line obtained by considering the clusters from all measurement locations simultaneously. In both cases, the results are fairly close, and Γ_{LS} is reported as the rate of decay of the inter-cluster energy versus delay. These results compare to values of 33.6 ns and 78.0 ns reported in [14] for two different buildings, and 60 ns reported in [8]. Thus the UWB signals recovered in this case exhibit a rate of decay that is comparable to some of the results reported previously, although it has been noted that this parameter is a strong function of the building architecture, as are many parameters of the propagation channel. These results allow for comparison against other experiments reported in the literature and for the derivation of a common parameter, the decay exponent, Γ.

Plots of the intra-cluster rate of decay, i.e., the rate at which the recovered energy in individual signal arrivals within a cluster falls off as a function of the delay (also called the ray decay rate [8], [14]) are shown below in Figure 13. The absolute deviation between the mean and median of the results from each measurement location and the least-squares fit to all of the recovered signal information is larger here, excluding the results at locations A and E. The results generated by considering the energy in the recovered waveform and the results from considering the amplitude only are so close that only the former is shown.

In [14], very different results are found for the inter-cluster decay exponent γ, depending on the building in which the measurements were conducted. In one building (cinderblock), a value of 28.6 ns is reported for γ, while in another building (steel frame and gypsum board) γ is found

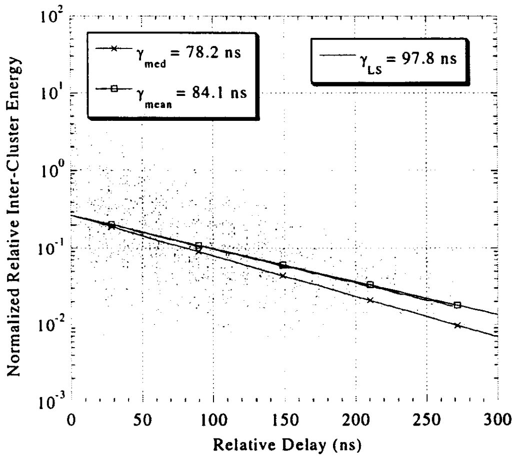

Fig. 13. Intra-cluster loss vs. relative delay when considering the energy in the recovered waveforms.

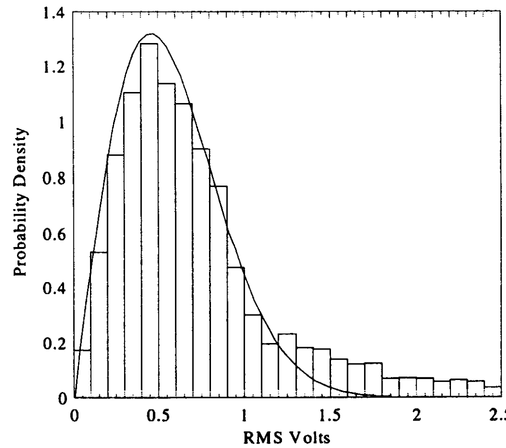

Fig. 14. Distribution of the arrival energy deviation from the mean, with a Rayleigh density overlayed.

to be 82.2 ns. Another reference, [8] reported a γ of 20 ns. The values for γ derived here for the UWB propagation channel are in the same neighborhood as those reported for the steel-frame and gypsum board building in [14].

The cluster decay rate Γ and the ray decay rate γ obtained here can be interpreted for the environment in which the measurements were made. Figure 3 indicates that with the exception of the measurements at locations F1 and F2, at least one wall separates the transmitter and the receiver. Each cluster can be viewed as a path that exists between the transmitter and the receiver along which signals propagate. This cluster path is generally a function of the architecture of the building itself. The component arrivals within a cluster vary because of secondary effects, e.g. reflections off of furniture or other objects. Our interpretation is that the primary source of degradation in the propagation through the features of the building is captured in the decay exponent Γ. Relative effects between paths in the same cluster do not always involve the penetration of additional obstructions or additional reflections, and therefore tend to contribute less to the decay of the component signals.

A Rayleigh distribution has been shown [8], [14] to provide a good fit to the deviation of the arrival energy from the mean curve, where the Rayleigh probability density function is given by

$$f_x(x) = \frac{x}{\alpha^2} e^{-\frac{x^2}{2\alpha^2}}$$

A histogram of the deviation values is shown in Figure 14, with a Rayleigh density with $\alpha = 0.46$ overlaid on top of the recovered distribution. This distribution represents the best-fit to the recovered UWB data when considering the Rayleigh, lognormal, Nakagami-m and Rician distributions as possibilities.

Consider next the angle-of-arrival properties of the cluster model. Assuming again the separable impulse response of equation (11), the model proposed in [14] to describe the angular impulse response is

$$h(\theta) = \sum_{l=0}^{\infty} \sum_{k=0}^{\infty} \beta_{kl} \delta(\theta - \Theta_l - \omega_{kl}) \tag{12}$$

where β_{kl} is the amplitude of the k^{th} arrival in the l^{th} cluster, Θ_l is the mean azimuth angle-of-arrival of the l^{th} cluster and ω_{kl} is the azimuth angle-of -arrival of the k^{th} arrival in the l^{th} cluster, relative to Θ_l. It is proposed in [14] that Θ_l is distributed uniformly in angle, and ω_{kl} is distributed according to a zero-mean Laplacian distribution,

$$p(\theta) = \frac{1}{\sqrt{2}\sigma} e^{-|\sqrt{2}\theta/\sigma|} \tag{13}$$

The recovered rays, i.e., intra-cluster arrivals, were tested against truncated Gaussian and Laplacian densities. It was determined that the relative azimuth arrival angles of the recovered UWB signals were best fit to a Laplacian density, with a standard deviation, σ, of 38°. The recovered signal information and the best-fit distribution are shown in Figure 15 at 1° of resolution.

These distributions compare with standard deviations on the Laplacian density of 25.5° and 21.5° reported in [14] as the best fit to the recovered angular information for two different buildings. It is likely that this parameter is a function of the building architecture, which again would suggest that further propagation studies are needed to determine whether the results presented here are typical. It is also possible that the difference in the results is due in part to the fractional bandwidth and center frequency of the UWB waveforms used in this study. The penetration properties of these signals, including the larger γ, might lead to the detection of responses that would remain undetected at if transmitted at a single frequency or over a smaller frequency range.

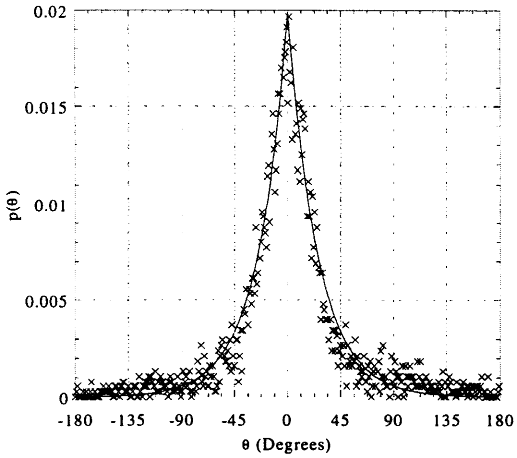

Fig. 15. Ray arrival angles at 1° of resolution and a best fit Laplacian density with σ=38°

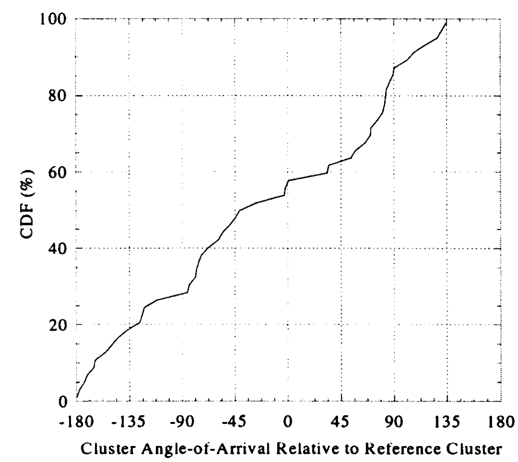

Fig. 16. Distribution of the cluster azimuth angle-of-arrival, relative to the reference cluster.

It was found in [14] that the relative cluster azimuth arrival angles were approximated by a uniform distribution over all angles. The recovered cluster angles in this work are shown in Figure 16, relative to the reference cluster angle-of-arrival, where the reference cluster is taken to be the first cluster to arrive in time, for each measurement location. This distribution is also approximately uniform, although it is noted that no clusters were reported to exist at angles above approximately 135°. It is conjectured that if more measurements were taken, angles would occur in this region, and this function would tend to more closely approximate a uniform distribution.

Finally, to complete this model of the UWB propagation channel, based on the multipath clustering phenomenon, the rates of the cluster and the ray arrivals must be determined. The inter-arrival times are hypothesized [14] to follow exponential rate laws, given by

$$p\left(T_l\,|T_{l-1}\right) = \Lambda e^{-\Lambda(T_l - T_{l-1})} \tag{14}$$

$$p\left(\tau_{kl}\,|\tau_{k-1,l}\right) = \lambda e^{-\lambda(T_l - T_{l-1})} \tag{15}$$

where Λ is the cluster arrival rate and λ is the ray arrival rate. Following this model, the best fit exponential distributions, parameterized on Λ and λ were determined for the recovered UWB cluster and ray arrival times, respectively. The resulting plots are shown in Figure 17 and Figure 18. The ray arrival rate determined for the UWB signals was faster than that reported in either [14] or [8]. A ray arrival rate of $1/\lambda$=2.3 ns defined the best-fit exponential distribution for the ray arrival times over all measurement locations, while ray arrival rates of $1/\lambda$=5.1 ns and $1/\lambda$=6.6 ns were reported in [14] for the two different buildings. A ray arrival rate of $1/\lambda$=5.0 ns was given in [8]. Several reasons are possible for the faster arrival rate. First, it may be due in part to the building architecture. Second, the fractional bandwidth of the UWB signals and the post-processing algorithms permit multipath time resolution on the order of 1 ns. The measurement equipment used in [14] allowed a time resolution on the incident signals of about 3 ns. Also shown in Figure 17 is a curve which represents the best-fit exponential to ray arrival times of greater than 8 ns, although this represents less than 10% of the values.

A cluster arrival rate of $1/\Lambda$=45.5 ns was found to define the best-fit exponential distribution in the UWB signal propagation model. This value is larger than the cluster arrival rates of 16.8 ns and 17.3 ns reported in [14], but less than the 300 ns given in [8]. Again, several explanations are possible to describe the differences. They could be due to the difference in the fractional bandwidths of the signals involved, the sensitivity of the measurement equipment or the building architecture. As discussed above, they could also be due to the orientation of the transmitter and receiver in the building.

The model parameters derived herein for the UWB signal propagation model and a comparison with the earlier work in [8], [14] are summarized in Table I.

TABLE I
COMPARISON OF CHANNEL MODELS

Parameter	UWB	Spencer et al.	Spencer et al.	Saleh-Valenzuela
Γ	27.9 ns	33.6 ns	78.0 ns	60 ns
γ	84.1 ns	28.6 ns	82.2 ns	20 ns
$1/\Lambda$	45.5 ns	16.8 ns	17.3 ns	300 ns
$1/\lambda$	2.3 ns	5.1 ns	6.6 ns	5 ns
σ	37°	25.5°	21.5°	-

VI. Conclusions

The main goal of this work was to develop an understanding of the indoor UWB propagation channel, including the time-of-arrival, angle-of-arrival and level distributions of a collection of received signals. To accomplish

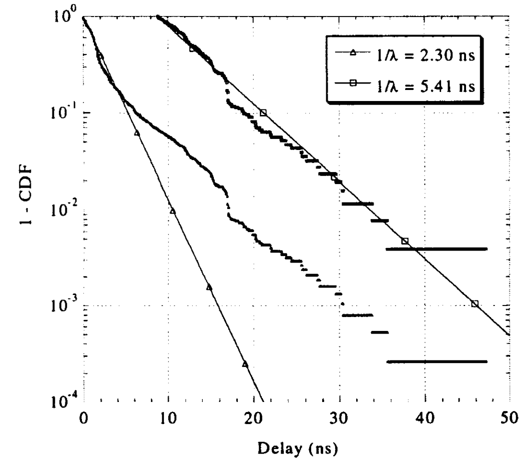

Fig. 17. Ray arrival rate for all measurement locations in the indoor UWB channel considered here.

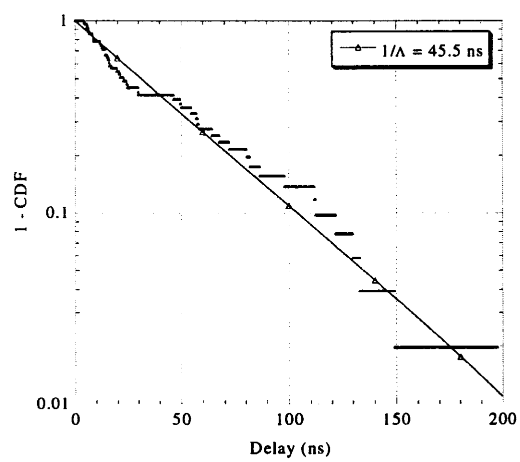

Fig. 18. Cluster arrival rate for all measurement locations in the indoor UWB channel considered here.

this, a set of algorithms suitable for processing UWB signals incident on an array of sensors was developed. These techniques were applied to the measured propagation data. From this, models for the propagation of UWB signals in an indoor channel were generated.

The channel models presented in this work are based on a set of measurement made at a number of locations within an office building. It has been noted that the geometry of the situation and the building architecture can have a significant effect on the received signals [15], [14]. Therefore, further work remains in the collection and processing of propagation data from different buildings,to increase the significance of and augment the results presented in this work. It is possible therefore, that the strongest contribution of this work is in the development of the processing algorithms, and that as more measurements are taken in different environments, the parameters of the UWB channel model presented here will change to reflect this new information.

References

[1] R. J.-M. Cramer, M.Z. Win, R.A. Scholtz, "Evaluation of the Multipath Characteristics of the Impulse Radio Channel," *Proc. of PIMRC '98*, vol. 2, p. 864-868.

[2] H. Hashemi, "The indoor radio propagation channel," *Proc. IEEE*, vol. 81, no. 7, pp. 943-968, July, 1993.

[3] J.A. Högbom, "Aperture Synthesis with a Non-Regular Distribution of Interferometer Baselines," *Astron. and Astrophys. Suppl. Ser.*, vol. 15, p.417-426, 1974.

[4] W. C. Jakes, *Microwave Mobile Communications*, IEEE Press, 1974.

[5] J.C. Liberti and T.S. Rappaport, *Smart Antennas for Wireless Communications: IS-95 and Third Generation CDMA Applications*, Prentice-Hall, Englewood Cliffs, New Jersey, 1999.

[6] J. Maloney et al., "Accurate Computation of the Radiation from Simple Antennas Using the Finite-Difference Time-Domain Method," IEEE Trans. On Antennas and Propagation, July 1990.

[7] D. Parsons, *The Mobile Radio Propagation Channel*, Halsted Press, 1992.

[8] A.A.M. Saleh and R.A. Valenzuela, "A statistical model for indoor multipath propagation", *IEEE JSAC*, vol. 5, no. 2, pp. 128-137, 1987.

[9] H. G. Schantz and L. Fullerton, "The Diamond Dipole: A Gaussian Impulse Antenna," Proceedings of the 2001 IEEE AP-S International Symposium, Boston, July 8-13,2001.

[10] R.A. Scholtz, "Multiple Access with Time-Hopping Impulse Modulation," in *Proc. Milcom*, Oct. 1993.

[11] R.A. Scholtz and M.Z. Win, "Impulse Radio," *Personal Indoor Mobile Radio Conference*, Helsinki, Finland, Sept. 1997, Printed in *Wireless Communications: TDMA vs. CDMA*, S.G. Glisic and P.A. Leppänen, eds., Kluwer Academic Publishers, 1997.

[12] R.A. Scholtz, R. J-M. Cramer, and M.Z. Win, "Evaluation of the Propagation Characteristics of Ultra-Wideband Communication Channels," Antennas and Propagation Society International Symposium, 1998, vol. 2, pp. 626-630.

[13] U.J. Schwarz, "Mathematical-statistical Description of the Iterative Beam Removing Technique (Method CLEAN)," *Astronomy and Astrophysics*, vol. 65, 1978, pp. 345-356.

[14] Q. Spencer, M. Rice, B. Jeffs, M. Jensen, "A Statistical Model for the Angle-of-Arrival in Indoor Multipath Propagation," *IEEE Vehicular Technology Conference*, IEEE, 1997, p. 1415-1419.

[15] Q. Spencer, B. Jeffs, M. Jensen, A. Swindlehurst, "Modeling the Statistical Time and Angle of Arrival Characteristics of an Indoor Multipath Channel," *IEEE Journal on Selected Areas in Communication*, vol. 18, no. 2, March 2000, p. 347-360.

[16] J.D. Taylor, *Introduction to Ultra-Wideband Radar Systems*, CRC Press, Boca Rator, FL, 1995.

[17] G. L. Turin, "Introduction to Spread Spectrum Antimultipath Techniques and their Application to Urban Digital Radio," Proc. IEEE, vol. 68, March 1980, pp. 328-354.

[18] R.G. Vaughan and N.L. Scott, "Super-Resolution of Pulsed Multipath Channels for Delay Spread Characterization," *IEEE Trans. Commun.*, vol. 47, no. 3, March 1999.

[19] M.Z. Win and R.A. Scholtz, "Impulse radio: How it works," *IEEE Commun. Lett.*, Feb. 1998.

[20] M.Z. Win, R.A. Scholtz, M.A. Barnes, "Ultra-Wideband Signal Propagation for Indoor Wireless Communications", *Proc IEEE Int. Conf. on Comm.*, June, 1997.

[21] R.A. Scholtz and M.Z. Win, "Impulse Radio," Personal Indoor Mobile Radio Conference, Helsinki, Finland, Sept. 1997. Printed in ireless Communications: TDMA versus CDMA, S. G. Glisic and p. A. Leppänen, eds., Kluwer Academic Publishers, 1997.

Ranging in a Dense Multipath Environment Using an UWB Radio Link

Joon-Yong Lee and Robert A. Scholtz

Abstract— **A time of arrival (ToA) based ranging scheme using an ultra-wideband (UWB) radio link is proposed. This ranging scheme implements a search algorithm for the detection of direct path signal in the presence of dense multipath, utilizing deterministic maximum likelihood (DML) estimation. Models for critical parameters in the algorithm are based on statistical analysis of propagation data, and the algorithm is tested on another independent set of propagation measurements. The proposed UWB ranging system uses a correlator and a parallel sampler with a high speed measurement capability in each transceiver to accomplish two-way ranging between them in the absence of a common clock.**

I. Introduction

THE fine time resolution of ultra-wideband (UWB) signals enables potential applications in high-resolution ranging. The novel aspect of UWB ranging is the fact that the multipath time-spread in many channels of interest is often 100 to 1000 times the inherent time resolution of the UWB signal detected in a matched-filter receiver. Detection of the direct path signal in the presence of dense multipath, which determines ranging quality, becomes a different kind of problem in this case. Multipath resolution techniques in narrowband systems have been well developed [8], [9]. Win and Scholtz [2] introduced a maximum likelihood (ML) detector for multipath in UWB propagation measurements and Cramer et al. [4], [5], [6] used the CLEAN algorithm to develop a UWB channel model involving angle of arrival (AoA) as well as time of arrival (ToA).

This paper introduces a time-of-arrival (ToA) measurement algorithm utilizing deterministic maximum likelihood (DML) estimation for the detection of the direct-path signal. Multipath delay and amplitude parameters appearing in this algorithm are modeled statistically from propagation data, and the algorithm is tested on an independent set of propagation measurements. Probabilistic analysis of different kinds of errors using these statistical models provides a way of determining the thresholds used in the ToA algorithm, as well as estimating the algorithm's performance. We conclude by presenting the schematic design of an UWB ranging system with a high-speed measurement capability and a two-way ranging technique that utilizes this algorithm.

This work was supported by the Office of Naval Research under Contract No. N00014-00-0221.

Joon-Yong Lee is a graduate student associated with the Ultra-Wideband Radio Laboratory at University of Southern California, Los Angeles, CA 90089-2560 USA (email:joonyong@usc.edu).

Dr. Robert A. Scholtz is Professor of Electrical Engineering, University of Southern California, Los Angeles, CA 90089-2560 USA (email:scholtz@usc.edu).

II. Propagation Measurement

A set of indoor propagation measurements was conducted at the University of Southern California to test the ToA algorithm presented in the next section. Pulses with a sub-nanosecond width were transmitted with one microsecond spacing and measured with a digital sampling scope. The antennas were vertically polarized diamond dipoles [10], approximately 5 feet above the floor. The sampling rate of the measured signal is 20.5 GHz. Sampled waveforms were averaged over 512 sweeps to acquire a higher signal-to-noise ratio (SNR).

Figure 1 is the floor plan of the building where the measurements were taken. Signals were measured at 18 different locations while the transmitter was fixed in the laboratory. At location 1, the signal was measured with a visually clear line-of-sight (LoS) and used to calibrate the arrival time of the direct path signal. The other 17 signals were measured with a blocked LoS. At location 16, 17, and 18, the LoS path was blocked by an elevator (a metallic structure), so the direct path signal could not be measured while multipath could be observed.

Figure 2 shows the samples of signals taken at location 1, 4, and 14, respectively. Notice that the signals shown in the second and the third plot have stronger multipath components than the direct path signal. In these cases, if a ranging system synchronizes with the strongest signal component for the purpose of range estimation, a large-scale error will occur. The presence of reflected signals that are stronger than the direct path signal makes ranging to

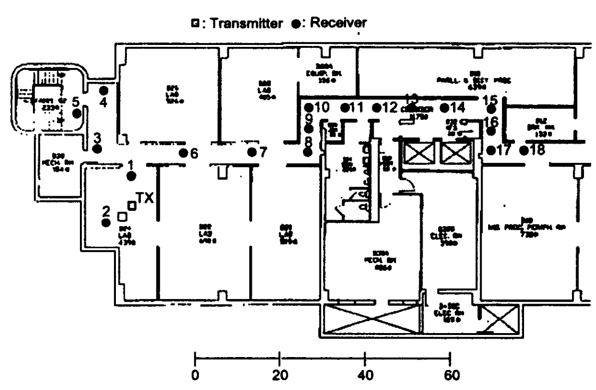

Fig. 1. Basement floor plan of the building where the experiments were conducted. Interior walls are metal stud and dry wall construction. Circular marks stand for the locations of the receiving antenna and the rectangular mark indicates the tranmitting antenna's location.

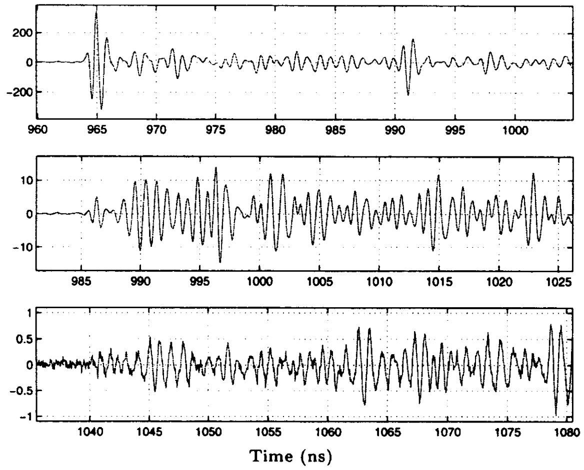

Fig. 2. Measured signals at location 1, 4, and 14. The vertical axis indicates signal strength in millivolts. The vertical scales of each plot are different, indicating differences in channel attenuation. The signal shown in the first plot was measured with a clear LoS and the others were measured in the presence of LoS blockages.

the full capabilities of ultra-wideband signals challenging.

III. Detection of Direct Path Signals

In this paper the direct path signal is assumed to be the earliest arrival at the receiver. When the straight-line path from transmitter to receiver is in fact a viable propagation path, ToA estimation of the direct path signal is useful for ranging. As shown in the signals of Figure 2, the direct path signal is not always the strongest in the presence of a visual LoS blockage. The ToA algorithm in this section does not assume that the direct path always supplies the strongest response.

A. Signal Representation

When a single pulse is transmitted, the received signal is composed of direct path signal, reflected signals, noise, and interference [1]. So the received signal $r_{\mathrm{m}}(t)$ can be represented by

$$r_{\mathrm{m}}(t) = a_{\mathrm{d}} s(t-\tau_{\mathrm{d}}) + \sum_{n=1}^{L} a_n s(t-\tau_n) + n_{\mathrm{m}}(t), \quad (1)$$

where $\tau_{\mathrm{d}} < \tau_1 < \tau_2 < \cdots < \tau_L$. The parameters τ_{d} and a_{d} are the arrival time and strength of the direct path signal, respectively, and τ_n and a_n are those of the n^{th} reflected component. The waveform $s(t)$ denotes the the canonical single-path signal, used as a correlator template, with a width of T_{p} seconds. The number of multipath signals L is unknown *a priori*. The noise $n_{\mathrm{m}}(t)$ is assumed to be additive white Gaussian, and interference is assumed to be zero.

Let τ_{peak} and a_{peak} be the arrival time and amplitude of the strongest path and assume these have been determined by correlation. Then $r_{\mathrm{s}}(t)$, a normalized and shifted version of $r_{\mathrm{m}}(t)$, can be represented by

$$\begin{aligned}
r_{\mathrm{s}}(t) &= \frac{1}{|a_{\mathrm{peak}}|} r_{\mathrm{m}}(t+\tau_{\mathrm{peak}}) & (2)\\
&= \rho s(t+\delta) + \sum_{n}^{L} \alpha_n s(t+\beta_n) + n_{\mathrm{s}}(t), & (3)\\
&= \rho s(t+\delta) + \sum_{\beta_n \ge 0} \alpha_n s(t+\beta_n) + \sum_{\beta_n < 0} \alpha_n s(t+\beta_n) & \\
&+ n_{\mathrm{s}}(t), & (4)
\end{aligned}$$

where

$$\left\{ \begin{array}{lcll}
\delta &=& \tau_{\mathrm{peak}} - \tau_{\mathrm{d}}, & \delta \ge 0, \\
\rho &=& a_{\mathrm{d}}/|a_{\mathrm{d}}|, & 0 < \rho \le 1, \\
\beta_n &=& \tau_{\mathrm{peak}} - \tau_n, & \delta > \beta_1 > \beta_2 > \cdots > \beta_L \\
\alpha_n &=& a_n/|a_{\mathrm{d}}|, & 0 < \alpha_n \le 1,\ \forall n \le L.
\end{array} \right. \quad (5)$$

The noise $n_{\mathrm{s}}(t)$ being a time-shifted version of $n_{\mathrm{m}}(t)$, is a white Gaussian noise signal. The third term in (4) represents the multipath components which arrive later than the peak path. To simplify the problem, let's restrict our observation to the portion of the signal prior to and including the arrival of the strongest path by truncating $r_{\mathrm{s}}(t)$. Let's define $r(t)$ as

$$\begin{aligned}
r(t) &= r_{\mathrm{s}}(t),\ t \le \frac{T_{\mathrm{p}}}{2} & (6)\\
&= \rho s(t+\delta) + \sum_{\beta_k \ge 0} \alpha_k s(t+\beta_k) + n(t),\ t \le \frac{T_{\mathrm{p}}}{2} & (7)\\
&= \rho s(t+\delta) + \sum_{k=1}^{M} \alpha_k s(t+\beta_k) + n(t),\ t \le \frac{T_{\mathrm{p}}}{2}, & (8)
\end{aligned}$$

where M is the number of signal components that arrived earlier than the peak component. If M is equal to 0, then $\delta = 0$, $\rho = 1$, and the second term in (8) is ignored. The noise $n(t)$ is white Gaussian noise (truncated to the interval $(-\infty, T_{\mathrm{p}}/2)$, whose correlation function is represented by

$$R_{\mathrm{N}}(\tau) = \sigma_{\mathrm{N}}^2 \cdot \delta_{\mathrm{D}}(\tau). \quad (9)$$

Assuming $r(t)$ is sampled, let's represent it as a vector of samples, namely,

$$\underline{r} = \rho \underline{s}_{\delta} + \sum_{k=1}^{M} \alpha_k \underline{s}_{\beta_k} + \underline{n}, \quad (10)$$

where $\underline{s}_{\beta}$ represents the vector of samples of $s(t+\beta)$ with a same length as $\underline{r}$. The noise vector $\underline{n}$ is a white gaussian vector whose correlation matrix R_{N} is given by

$$R_{\mathrm{N}} = \sigma_{\mathrm{N}}^2 \cdot I, \quad (11)$$

I being an identity matrix.

B. ToA Measurement Algorithm Using DML Estimation

In (10), δ is the parameter to be estimated, and ρ, M, $\underline{\alpha}^M$, and $\underline{\beta}^M$ are nuisance parameters, where $\underline{\alpha}^M$ and $\underline{\beta}^M$ are defined as

$$\begin{aligned}
\underline{\alpha}^M &= (\alpha_1, \alpha_2, \cdots, \alpha_M), & (12)\\
\underline{\beta}^M &= (\beta_1, \beta_2, \cdots, \beta_M). & (13)
\end{aligned}$$

Deterministic maximum-likelihood estimation treats all of these unknown parameters as deterministic and estimates δ to be

$$\hat{\delta} = \arg\max_{\delta} \Big[\max_{\rho, M, \underline{\alpha}, \underline{\beta}} f(\underline{r}|\delta, \rho, M, \underline{\alpha}^M, \underline{\beta}^M) \Big]. \tag{14}$$

Because $\underline{n}$ is a white Gaussian vector, this is equivalent to

$$\hat{\delta} = \arg\min_{\delta} \Big[\min_{\rho, M, \underline{\alpha}, \underline{\beta}} \|\underline{r} - \rho \underline{s}_{\delta} - \sum_{k=1}^{M} \alpha_k \underline{s}_{\beta_k}\|^2 \Big]. \tag{15}$$

Using (15) to estimate δ is computation-intensive because $2(M+1)$ unknown parameters are involved. To reduce computational complexity, an iterative nonlinear programming technique is employed, by which the unknown parameters are estimated in a sequential manner [2]. Specifically, the arrival time of each component signal is estimated individually while all other parameters are fixed.

Modification of the estimation criterion shown in (15) is done as follows. First, the duration of the search region for the time δ of arrival of the direct path signal is limited to prevent the probability of a false detection in the noise only portion of the observed signal from becoming too large. We define θ_δ as a limiting threshold on δ so that the direct path signal is searched over the portion of $r(t)$ satisfying $t \geq -\theta_\delta$. Secondly, a stopping rule is used to terminate the search, because the value of the norm in (15) generally continues to decrease with increasing M. The stopping rule is consists of applying a threshold on the relative path strength ρ. The iterative search process stops when no more paths satisfying $\rho \geq \theta_\rho$ are detected in the search region, where θ_ρ is the threshold of ρ. Thirdly, we skip the estimation of some nuisance parameters by ignoring the multipath components that arrive later than already detected paths. By doing this, we can speed up the search process. Following is a brief description of the ToA algorithm:

1. Let $n = 1$, $\omega_1 = 0$, and $\mu_{11} = 1$.
2. Increase n by 1.
3. Find ω_n which satisfies

$$\omega_n = \arg \max_{\omega_{n-1} < \omega < \theta_\delta} \big(\underline{r} - \sum_{i=1}^{n-1} \mu_{(n-1)i} \underline{s}_{\omega_i}\big)^t \underline{s}_{\omega}, \tag{16}$$

4. Find $(\mu_{n1}, \mu_{n2}, \cdots, \mu_{nn})$ such that

$$(\mu_{n1}, \mu_{n2}, \cdots, \mu_{nn}) = \arg \min_{\mu'_1, \cdots, \mu'_2} \|\underline{r} - \sum_{i=1}^{n} \mu'_i \underline{s}_{\omega_i}\|^2. \tag{17}$$

5. If $\mu_{nn} \geq \theta_\rho$, go to step 2. Otherwise proceed to the next step.
6. δ is estimated as $\hat{\delta} = \omega_{n-1}$.

IV. Statistical Modeling of Ranging Parameters

The thresholds, θ_δ and θ_ρ, which are used in the ToA algorithm have to be determined so that they satisfy a given performance criteria. One of the potential criteria is that the probability of error is minimized. For the purpose of error analysis, the parameters $\boldsymbol{\delta}$ and $\boldsymbol{\rho}$ which were defined in III-A were modeled statistically.

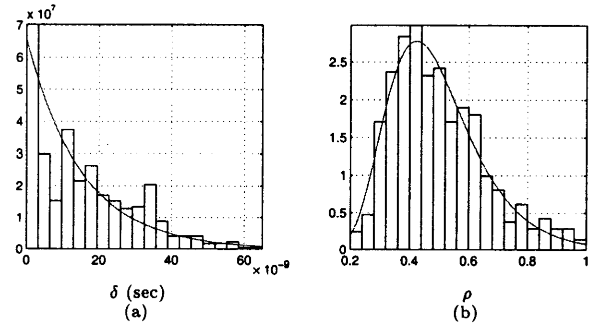

Fig. 3. Normalized histograms of (a) $\boldsymbol{\delta}$ and (b) $\boldsymbol{\rho}$ and approximation of marginal densities using curve-fitting.

A set of propagation data taken by Win [3] in an office building was used for this modeling. The values of δ's and ρ's of 622 signals which were measured with a blocked LoS were extracted using the ToA algorithm. The values of θ_δ and θ_ρ used in this process were 70ns and 0.2, respectively. Some large scale errors relative to the approximately known distance information were corrected by manually adjusting the thresholds. In 95 of 622 observed signals, the direct path signal was the strongest. So if we define P_0 as the probability that $\boldsymbol{\delta}$ is equal to 0 , it can be modeled by

$$P_0 = Pr(\boldsymbol{\delta} = 0) = Pr(\boldsymbol{\rho} = 1) = 0.1527. \tag{18}$$

Figure 3-(a) and (b) are normalized histograms of $\boldsymbol{\delta}$ and $\boldsymbol{\rho}$ which were produced with 527 signals that have a stronger reflected path than the direct path. By curve-fitting on this data, marginal densities of $\boldsymbol{\delta}$ and $\boldsymbol{\rho}$ can be modeled by

$$f_{\boldsymbol{\delta}}(\delta|\boldsymbol{\delta} \neq 0) = \frac{1}{\sigma_\delta} e^{-\delta/\sigma_\delta}, \ \delta > 0, \tag{19}$$

$$f_{\boldsymbol{\rho}}(\rho|\boldsymbol{\rho} \neq 1) = \frac{1}{\sqrt{2\pi} Q(-\mu/\sigma_\rho)\sigma_\rho \rho} e^{-(\ln \rho - \mu_\rho)^2/2\sigma_\rho^2}, \quad 0 < \rho < 1, \tag{20}$$

where $\sigma_\delta = 1.524 \times 10^{-8}$, $\sigma_\rho = 0.3220$, and $\mu_\rho = -0.7565$. The Q-function appearing in (20) is for normalization.

Independence between $\boldsymbol{\delta}$ and $\boldsymbol{\rho}$ was tested using a chi-squared test. Pearson's statistic χ^2 with 100 degrees of freedom, which was evaluated with the data set, is 117.2. According to the χ^2 distribution table, the critical value corresponding to a 10% significance level and 100 degrees of freedom is 118.5, which is greater than the value evaluated with data. So we can accept the hypothesis of independence between $\boldsymbol{\delta}$ and $\boldsymbol{\rho}$ with a 10% significance level [13], [14]. Based on this result, the joint density of $\boldsymbol{\delta}$ and $\boldsymbol{\rho}$ can be modeled by

$$f_{\boldsymbol{\delta\rho}}(\delta, \rho|\boldsymbol{\delta} \neq 0, \boldsymbol{\rho} \neq 1) = f_{\boldsymbol{\delta}}(\delta|\boldsymbol{\delta} \neq 0) \cdot f_{\boldsymbol{\rho}}(\rho|\boldsymbol{\rho} \neq 1)$$

$$= \frac{1}{\sqrt{2\pi}Q(-\mu/\sigma_\rho)\sigma_\delta\sigma_\rho\rho} \exp\left\{-\left[\frac{\delta}{\sigma_\delta} + \frac{(\ln\rho - \mu_\rho)^2}{2\sigma_\rho^2}\right]\right\}, \tag{21}$$

where $\delta > 0$, and $0 < \rho < 1$.

V. Error Analysis

Range estimation error can result from two major sources. One is ToA estimation error, and the other is any unknown propagation delay in a LoS blockage structure, which is difficult to estimate without a more thorough knowledge of the blockage. In this section, errors in ToA estimation of the direct path signal are analyzed probabilistically.

We can classify ToA errors into two categories. One is early false alarms which occur when a false detection in the noise-only portion of the signal is regarded as that of direct path signal. The other is a missed direct-path error, which occurs when the actual direct path signal is missed and a multipath signal is falsely declared to be direct path signal.

A. Probability of an Early False Alarm

An early false alarm probability P_{FA} can be expressed as

$$\begin{aligned} P_{\mathrm{FA}} &= Pr\left\{\sup_{\beta\in[-\theta_\delta,-\delta)} \frac{|\underline{n}^t\underline{s}_\beta|}{\|\underline{s}_0\|^2} > \theta_\rho \text{ and } \delta \le \theta_\delta\right\} &(22)\\ &= \int_0^{\theta_\delta} Pr\left\{\sup_{\beta\in[-\theta_\delta,-\delta)} \frac{|\underline{n}^t\underline{s}_\beta|}{\|\underline{s}_0\|^2} > \theta_\rho\right\} f_\delta(\delta|\delta\neq 0)d\delta \\ &\quad \cdot(1-P_0) + Pr\left\{\sup_{\beta\in[-\theta_\delta,0)} \frac{|\underline{n}^t\underline{s}_\beta|}{\|\underline{s}_0\|^2} > \theta_\rho\right\}\cdot P_0 &(23)\\ &= \int_0^{\theta_\delta} Pr\left\{\sup_{\beta\in[-\theta_\delta,-\delta)} \frac{|\underline{w}^t\underline{s}_\beta|}{\|\underline{s}_0\|^2} > \frac{\theta_\rho}{\sigma_{\mathrm{N}}}\right\} f_\delta(\delta|\delta\neq 0)d\delta \\ &\quad \cdot(1-P_0) + Pr\left\{\sup_{\beta\in[-\theta_\delta,0)} \frac{|\underline{w}^t\underline{s}_\beta|}{\|\underline{s}_0\|^2} > \frac{\theta_\rho}{\sigma_{\mathrm{N}}}\right\}\cdot P_0 &(24)\end{aligned}$$

where

$$\underline{w} = \frac{1}{\sigma_{\mathrm{N}}}\underline{n}. \tag{25}$$

Let's define the peak SNR as the ratio of the peak signal power to the noise power. This can be expressed as

$$\mathrm{SNR_p} = \frac{1}{\sigma_{\mathrm{N}}^2}, \tag{26}$$

because the signal was normalized to its peak strength. Substituting (26) into (24),

$$\begin{aligned} P_{\mathrm{FA}} &= \int_0^{\theta_\delta} Pr\left\{\sup_{\beta\in[-\theta_\delta,-\delta)} \frac{|\underline{w}^t\underline{s}_\beta|}{\|\underline{s}_0\|^2} > \theta_\rho\sqrt{\mathrm{SNR_p}}\right\} \\ &\quad \cdot f_\delta(\delta|\delta\neq 0)d\delta\cdot(1-P_0) \\ &\quad + Pr\left\{\sup_{\beta\in[-\theta_\delta,0)} \frac{|\underline{w}^t\underline{s}_\beta|}{\|\underline{s}_0\|^2} > \theta_\rho\sqrt{\mathrm{SNR_p}}\right\}\cdot P_0 &(27)\end{aligned}$$

Let's define γ and a random process $\boldsymbol{u}(\beta)$ as

$$\begin{aligned}\gamma &= \theta_\rho\cdot\sqrt{\mathrm{SNR_p}}, &(28)\\ \boldsymbol{u}(\beta) &= \frac{|\underline{w}^t\underline{s}_\beta|}{\|\underline{s}_0\|^2}. &(29)\end{aligned}$$

Substituting (28) and (29) into (27),

$$\begin{aligned} P_{\mathrm{FA}} = &\int_0^{\theta_\delta} Pr\left\{\sup_{\beta\in[-\theta_\delta,-\delta)} \boldsymbol{u}(\beta) > \gamma\right\} f_\delta(\delta|\delta\neq 0)d\delta \\ &\cdot(1-P_0) + Pr\left\{\sup_{\beta\in[-\theta_\delta,0)} \boldsymbol{u}(\beta) > \gamma\right\}\cdot P_0. \end{aligned} \tag{30}$$

$Pr\{\sup_{\beta\in[-\theta_\delta,-\delta)} \boldsymbol{u}(\beta) > \gamma\}$ can be modeled as a high level crossing probability of a random process $\boldsymbol{u}(\beta)$ at a level γ in a given time period $[-\theta_\delta,-\delta)$. This probability can be approximated by [11]

$$Pr\left\{\sup_{\beta\in[-\theta_\delta,-\delta)} \boldsymbol{u}(\beta) > \gamma\right\} \approx 1 - e^{-(\theta_\delta-\delta)/E(\boldsymbol{\lambda}_\gamma)}, \tag{31}$$

where $\boldsymbol{\lambda}_\gamma$ represents the time between a down-crossing and the next adjacent up-crossing at a given level γ. The expected value of $\boldsymbol{\lambda}_\gamma$ was simulated using a computer generated white Gaussian vector. The value of $\boldsymbol{\lambda}_\gamma$ for a given γ was observed over 100 occurrences and averaged. By curve-fitting on the simulation result, $E(\boldsymbol{\lambda}_\gamma)$ can be modeled by

$$E(\boldsymbol{\lambda}_\gamma) = C\cdot e^{B\gamma}, \tag{32}$$

where $B = 6.5757$ and $C = 1.375\times 10^{-11}$. Substituting (32) into (31),

$$Pr\left\{\sup_{\beta\in[-\theta_\delta,-\delta)} \boldsymbol{u}(\beta) > \gamma\right\} = 1 - \exp\left[-\frac{(\theta_\delta-\delta)}{C}e^{-B\gamma}\right] \tag{33}$$

Substituting (19) and (33) into (30), we get

$$\begin{aligned} P_{\mathrm{FA}} = &1 - (1-P_0)\frac{\sigma_\delta e^{-\theta_\delta/\sigma_\delta}}{\sigma_\delta - Ce^{B\gamma}} \\ &-\frac{P_0\sigma_\delta - Ce^{B\gamma}}{\sigma_\delta - Ce^{B\gamma}}\exp\left[-\frac{\theta_\delta}{C}e^{-B\gamma}\right]. \end{aligned} \tag{34}$$

Substituting (28) into (34),

$$\begin{aligned} P_{\mathrm{FA}} = &1 - (1-P_0)\frac{\sigma_\delta e^{-\theta_\delta/\sigma_\delta}}{\sigma_\delta - Ce^{B\theta_\rho\sqrt{\mathrm{SNR_p}}}} \\ &-\frac{P_0\sigma_\delta - Ce^{B\theta_\rho\sqrt{\mathrm{SNR_p}}}}{\sigma_\delta - Ce^{B\theta_\rho\sqrt{\mathrm{SNR_p}}}}\exp\left[-\frac{\theta_\delta}{C}e^{-B\theta_\rho\sqrt{\mathrm{SNR_p}}}\right]. \end{aligned} \tag{35}$$

B. Probability of a Missed Direct Path Error

The probability P_{M} of a missed-direct-path error can be evaluated by computing

$$\begin{aligned} P_{\mathrm{M}} &= Pr(\delta > \theta_\delta \text{ or } \rho < \theta_\rho) \\ &= 1 - Pr(0\le\delta\le\theta_\delta \text{ and } \theta_\rho\le\rho\le 1) \\ &= 1 - P_0 - (1-P_0)\int_{\theta_\rho}^1\int_0^{\theta_\delta} f_{\delta\rho}(\delta,\rho|\delta\neq 0)d\delta d\rho. \end{aligned} \tag{36}$$

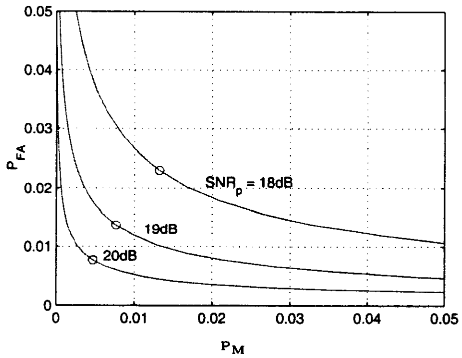

Fig. 4. Early false alarm probability vs. probability of a missed direct path for different peak SNR's. θ_δ = 100ns and θ_ρ was varied. At the circular mark on each curve, probability of error is minimized.

Substituting (21) into (36),

$$P_M = (1 - P_0)\left[1 - (1 - e^{-\theta_\delta/\sigma_\delta})\left(1 - \frac{Q(\frac{\ln\theta_\rho - \mu_\rho}{\sigma_\rho})}{Q(\frac{-\mu_\rho}{\sigma_\rho})}\right)\right] \quad (37)$$

Figure 4 is a plot of P_{FA} vs. P_M for different values of peak SNR. The value of θ_δ was fixed at 100ns and these two error probabilities were calculated for various θ_ρ. The circular mark on each curve represents the points where the sum of the two error probabilities is minimized.

VI. Test on Measured Data

Figure 5 shows of test results of the ToA algorithm on the signals measured at location 9 and 13. In each example, the upper plot is the measured waveform and the lower one shows the reconstructed signal with the paths detected in the ToA algorithm. The value of θ_ρ was determined so that the total probability of error ($P_{FA} + P_M$) is minimized while θ_δ was fixed. The vertical line appearing in each plot indicates the expected arrival time of the direct-path signal in the presence of a clear LoS path, based on physical range measurements. We can observe a few nanoseconds of discrepancy between this line and signal frontend in both examples. This probably is caused by excessive propagation delay in the LoS blockage. This unknown delay makes it difficult to measure the true arrival time of direct path.

Figure 6 shows the range estimation errors incurred in this test at the locations marked in Figure 1. Notice that larger errors occurred at long ranges, probably because the structure of LoS blockage was more complex at these locations.

VII. Design of UWB Ranging system

A. System Description

Withington et al. [7] introduced an UWB scanning receiver system which, using two correlators, has the capability of communication and channel pulse response measurement. The block diagram of an UWB ranging system using a correlator and a parallel sampler is shown in Figure 7. When the signal is received, the correlator synchronizes

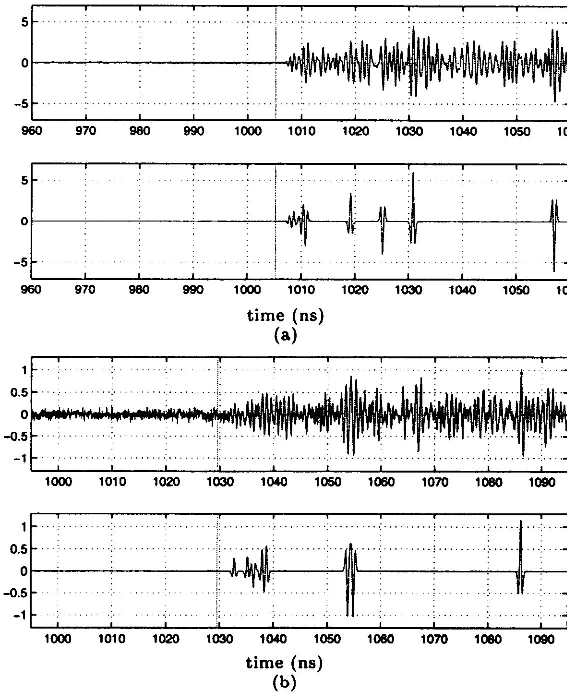

Fig. 5. ToA algorithm tested on measured signal at location 9 and 13. The vertical scale is in millivolts. Vertical line in each plot show the ToA of the direct path signal based on true measured range, assuming the presence of a clear LoS. θ_δ = 100ns and θ_ρ was determined so that $P_{FA} + P_M$ is minimized. The values of θ_ρ used in each test are (a)0.050 and (b)0.154.

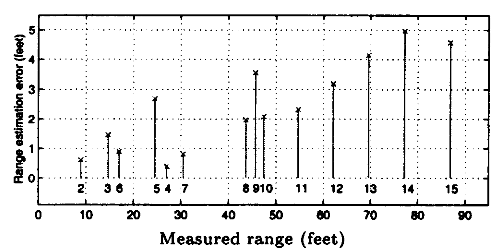

Fig. 6. Range estimation errors (estimated range - measured range). The numbers are the index of measurement positions. Ranging errors shown in this plot contains excessive propagation delay in the blockage structures.

with the signal, U_n being the time-tracking point in the n^{th} time frame. Once the correlator is locked, the parallel sampler starts sampling the incoming signal under the time control of a trigger signal. The trigger time V_n in n^{th} time frame is controlled relative to the tracking time U_n. This parallel sampler is composed of a bank of N_R individual samplers and N_R analog-to-digital converters (ADC). Each individual sampler takes N_S samples per time frame at a sampling rate of $1/T_S$ Hz. The offset in the sampling times of two adjacent individual samplers is ϕ_s, which satisfies

$$\phi_s \cdot N_R = T_S. \quad (38)$$

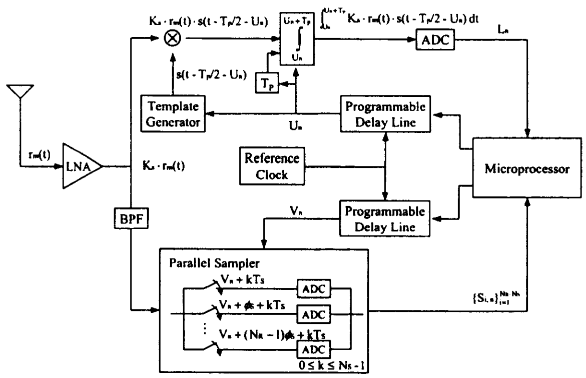

Fig. 7. Receiver schematic of UWB ranging system.

Total $N_S \cdot N_R$ samples are taken in each time frame by this parallel sampler and the overall sampling frequency is $1/\phi_s$ Hz. To acquire an acceptable SNR, each sample is integrated over several time frames. By changing the sampler's trigger time relative to the time-tracking point, the sampling frequency of the measured signal can be increased.

B. Two-Way Ranging Scheme

A UWB ranging system estimates the range by measuring signal round-trip time without a common timing reference. This ranging scheme uses a two-way remote synchronization technique [12] employed in satellite systems. Figure 8 is the timing diagram of this approach. A pair of UWB radios are time multiplexed with a period of T_M. Each radio switches between a transmission mode and a reception mode every $T_M/2$ sec. Radio 1 transmits signal 1 which is a train of pulses without modulation. It is received by radio 2 and signal 1$'$ denotes the captured signal. The time-multiplex period T_M is assumed to be large enough relative to the temporal profile of the received signal so that it does not affect the next transmission. The delay between transmission and reception of this signal is $\tau_{\text{prop}} + \tau_{\text{off},1}$, where τ_{prop} is the propagation time and $\tau_{\text{off},1}$ represents the time offset between the locked path and the direct path. With a known delay of $T_M/2$ from the front end of signal 1$'$, radio 2 transmits signal 2 and it is captured by radio 1. Signal 2$'$ denotes the captured signal by radio 1. Similarly, a delay of $\tau_{\text{prop}} + \tau_{\text{off},2}$ exists in this direction. The structures of signal 2 and signal 2$'$ are similar to those of signal 1 and signal 1$'$, respectively. Radio 1 can measure the signal round-trip time, τ_{round}, which is

$$\tau_{\text{round}} \approx 2\tau_{\text{prop}} + \frac{T_M}{2} + \tau_{\text{off},1} + \tau_{\text{off},2}. \qquad (39)$$

Then the signal propagation time can be approximated by

$$\tau_{\text{prop}} \approx \frac{\tau_{\text{round}} - T_M/2 - \tau_{\text{off},1} - \tau_{\text{off},2}}{2}. \qquad (40)$$

Radio 2 informs radio 1 of $\tau_{\text{off},1}$ afterwards with a few bits of information so that radio 1 can evaluate the signal propagation time. If the SNR of the measured signal is not large enough, the two radios increase the signal measurement time to acquire an acceptable SNR.

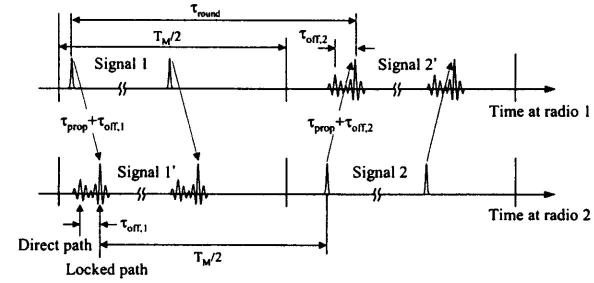

Fig. 8. Evaluation of the signal round-trip time.

VIII. Conclusions

According to tests on the propagation data, there exists excessive propagation delay in the LoS blockage material which is considerable when the structure of this blockage is complex. This excessive propagation delay is a limiting factor in UWB ranging performance through materials.

IX. Acknowledgements

The authors would like to thank Profs. Keith Chugg and Urbashi Mitra for their suggestions.

References

[1] R. A. Scholtz et al., "UWB radio deployment challenges," in *Proc. PIMRC '2000*, 2000, vol. 1, pp. 620–625.

[2] M. Z. Win and R. A. Scholtz, "Energy capture vs. correlator resources in ultra-wide bandwidth indoor wireless communications channels," in *Proc. Milcom '97*, Nov 1997.

[3] M.Z. Win and R. A. Scholtz, "Ultra-wide bandwidth signal propagation for indoor wireless communications," in *Proc. ICC '97*, Jun 1997.

[4] J. M. Cramer, R. A. Scholtz, and M.Z. Win, "Spatio-temporal diversity in ultra-wideband radio," in *Proc. WCNC '99*, 1999, vol. 2, pp. 888–892.

[5] J. M. Cramer, M.Z. Win, and R. A. Scholtz, "Evaluation of multipath characteristics of the impulse radio channel," in *Proc. PIMRC '98*, 1998, vol. 2, pp. 864–868.

[6] J. M. Cramer, R. A. Scholtz, and M. Z. Win, "Evaluation of an ultra-wideband propagation channel," to be published, 2002.

[7] P. Withington, R. Reinhardt, and R. Stanley, "Preliminary results of an ultra-wideband (impulse) scanning receiver," in *Proc. MILCOM'99*, 1999.

[8] T. G. Manickam, R. J. Vaccaro, and D. W. Tufts, "A least-squares algorithm for multipath time-delay estimation," *IEEE Trans. Signal Processing*, vol. 42, no. 11, pp. 3229–3233, Nov. 1994.

[9] Ilan Ziskind and Mati Wax, "Maximum likelihood localization of multiple sources by alternating projection," *IEEE Trans. Acoustics, Speech, and Signal Processing*, vol. 36, no. 10, pp. 1553–1560, 1988.

[10] H. G. Schantz and L. Fullerton, "The diamond dipole: A gaussian impulse antenna," in *Proceedings of the 2001 IEEE AP-S International Symposium*, Boston, July 2001.

[11] James R. Rice, "First-occurrence time of high-level crossings in a continuous random process," *Jour. Acoust. Soc. Amr.*, vol. 39, no. 2, pp. 323–335, 1966.

[12] W.C. Lindsey and M.K. Simon, *Phase and doppler measurements in two-way phase-coherent tracking systmes*, Dover Pubs, 1991.

[13] E. L. Lehmann, *Nonparametrics: Statistical Methods Based on Ranks*, McGraw-Hill Book Company, San Francisco, 1975.

[14] Priscilla E. Greenwood and Mikhail S. Nikulin, *A Guide to Chi-Squared Testing*, A Wiley-Interscience Publication, New York, 1975.